

# Plasma Interactions with Icy Bodies in the Solar System

**Jesper Lindkvist**

Doctoral Thesis



**Swedish Institute of Space Physics**  
Kiruna, 2016



**Department of Physics**  
Umeå, 2016

ISBN 978-91-982951-1-5

ISSN 0284-1703

Electronic version available on <http://umu.diva-portal.org/>

Printed by: Universitetsservice US-AB

Stockholm, Sweden, 2016

*Tillägnad min mormor*



# Contents

<b>Contents</b>	<b>i</b>
<b>Abstract</b>	<b>iii</b>
<b>List of included papers</b>	<b>v</b>
<b>List of figures</b>	<b>vii</b>
<b>List of acronyms</b>	<b>ix</b>
<b>Sammanfattning</b>	<b>xi</b>
<b>1 Introduction</b>	<b>1</b>
1.1 Modelling space plasmas . . . . .	2
<b>2 Space plasma physics</b>	<b>3</b>
2.1 Definition of a plasma . . . . .	3
2.1.1 Debye shielding . . . . .	4
2.1.2 Plasma parameter . . . . .	6
2.1.3 Plasma frequency . . . . .	7
2.2 Single particle motion . . . . .	8
2.2.1 Field equations . . . . .	8
2.2.2 Equation of motion . . . . .	9
2.2.3 Analytical solution to the equation of motion . . . . .	10
2.3 Velocity space distribution . . . . .	20
2.3.1 Macroscopic quantities . . . . .	20
2.3.2 Maxwellian distribution . . . . .	21
2.3.3 Neutral non-collisional outflow . . . . .	25
2.4 Magnetic induction . . . . .	27
2.4.1 Time-varying magnetic field . . . . .	27
2.4.2 Plasma-induced currents . . . . .	29
2.5 Ion waves . . . . .	30
2.5.1 Electrostatic waves . . . . .	30
2.5.2 Electromagnetic waves . . . . .	31

<b>3</b>	<b>Hybrid modelling of plasmas</b>	<b>33</b>
3.1	Hybrid approximations . . . . .	33
3.2	Hybrid equations . . . . .	35
3.3	Resistivity . . . . .	36
3.3.1	Coulomb collisions . . . . .	36
3.3.2	Implementation . . . . .	36
3.4	Time step constraints . . . . .	38
3.4.1	Waves . . . . .	38
3.4.2	Oscillations . . . . .	38
3.4.3	Particles . . . . .	39
3.4.4	Diffusion . . . . .	39
3.4.5	Massless electrons . . . . .	39
3.4.6	Gravity . . . . .	40
3.5	Smoothing techniques . . . . .	40
3.5.1	Vacuum regions . . . . .	41
3.5.2	Oscillations in the plasma . . . . .	41
3.5.3	Hyperresistivity . . . . .	42
3.6	Magnetic induction model . . . . .	43
3.7	Neutral release model . . . . .	43
3.7.1	Implementation . . . . .	44
3.7.2	Neutral distribution . . . . .	45
3.8	Haser model . . . . .	47
3.8.1	Implementation . . . . .	48
3.9	Averaging techniques . . . . .	48
3.10	Sub-Alfvénic interaction . . . . .	50
3.10.1	Subsonic interaction . . . . .	50
<b>4</b>	<b>Plasma interactions with icy bodies</b>	<b>51</b>
4.1	Solar wind . . . . .	52
4.2	Comet 67P/CG . . . . .	53
4.2.1	Evolution of the comet interaction . . . . .	54
4.3	Ceres . . . . .	60
4.4	Callisto . . . . .	62
4.4.1	The magnetosphere of Jupiter . . . . .	63
4.4.2	Supersonic interaction . . . . .	64
4.5	Future work . . . . .	68
4.5.1	Comet 67P/CG . . . . .	68
4.5.2	Ceres . . . . .	68
4.5.3	Callisto . . . . .	68
4.6	Conclusions . . . . .	69
<b>5</b>	<b>Summary of included papers</b>	<b>71</b>
	<b>Acknowledgements</b>	<b>75</b>
	<b>Bibliography</b>	<b>77</b>

# Abstract

Here I study the “plasma interactions with icy bodies in the solar system”, that is, my quest to understand the fundamental processes that govern such interactions. By using numerical modelling combined with in situ observations, one can infer the internal structure of icy bodies and their plasma environments.

After a broad overview of the laws governing space plasmas a more detailed part follows. This contains the method on how to model the interaction between space plasmas and icy bodies. Numerical modelling of space plasmas is applied to the icy bodies Callisto (a satellite of Jupiter), the dwarf planet Ceres (located in the asteroid main belt) and the comet 67P/Churyumov-Gerasimenko.

The time-varying magnetic field of Jupiter induces currents inside the electrically conducting moon Callisto. These create magnetic field perturbations thought to be related to conducting subsurface oceans. The flow of plasma in the vicinity of Callisto is greatly affected by these magnetic field perturbations. By using a hybrid plasma solver, the interaction has been modelled when including magnetic induction and agrees well with magnetometer data from flybys (C3 and C9) made by the *Galileo* spacecraft. The magnetic field configuration allows an inflow of ions onto Callisto’s surface in the central wake. Plasma that hits the surface knocks away matter (sputtering) and creates Callisto’s tenuous atmosphere.

A long term study of solar wind protons as seen by the *Rosetta* spacecraft was conducted as the comet 67P/Churyumov-Gerasimenko approached the Sun. Here, extreme ultraviolet radiation from the Sun ionizes the neutral water of the comet’s coma. Newly produced water ions get picked up by the solar wind flow, and forces the solar wind protons to deflect due to conservation of momentum. This effect of mass-loading increases steadily as the comet draws closer to the Sun. The solar wind is deflected, but does not lose much energy. Hybrid modelling of the solar wind interaction with the coma agrees with the observations; the force acting to deflect the bulk of the solar wind plasma is greater than the force acting to slow it down.

Ceres can have high outgassing of water vapour, according to observations by the Herschel Space Observatory in 2012 and 2013. There, two regions were identified as sources of water vapour. As Ceres rotates, so will the source regions. The plasma interaction close to Ceres depends greatly on the source location of water vapour, whereas far from Ceres it does not. On a global scale, Ceres has a comet-like interaction with the solar wind, where the solar wind is perturbed far downstream of Ceres.



## List of included papers

This thesis is based on the following papers, which are referred to in the text by their Roman numerals.

### I

LINDKVIST, J., HOLMSTRÖM, M., KHURANA, K. K., FATEMI, S., AND BARABASH, S. Callisto plasma interactions: Hybrid modeling including induction by a subsurface ocean. *Journal of Geophysical Research: Space Physics* 120, 6 (2015), 4877–4889.

### II

PFLEGER, M., LINDKVIST, J., LAMMER, H., HOLMSTRÖM, M., VORBURGER, A., LICHTENEGGER, H. I. M., WURZ, P., AND BARABASH, S. 3D-modeling of Callisto’s sputtered exosphere environment. *Journal of Geophysical Research: Planets* (2016).  
*Submitted*

### III

LINDKVIST, J., HOLMSTRÖM, M., FATEMI, S., WIESER, M., AND BARABASH, S. Ceres interaction with the solar wind. *Geophysical Research Letters* (2016).  
*Submitted*

### IV

BEHAR, E., LINDKVIST, J., NILSSON, H., HOLMSTRÖM, M., STENBERG-WIESER, G., RAMSTAD, R., AND GÖTZ, C. Light mass loading of the solar wind at 67P/Churyumov-Gerasimenko. *Astronomy & Astrophysics* (2016).  
*Submitted*

Reprints were made with permission from the publishers.



## List of figures

2.1	Number density and precipitating flux at Callisto's surface . . . . .	18
2.2	Number density and precipitating flux versus the ram angle for Callisto . . . . .	19
2.3	Non-drifting Maxwellian velocity distribution function . . . . .	22
2.4	Discretised Maxwellian velocity distribution function . . . . .	23
3.1	Weighting of average quantities at an arbitrary position . . . . .	49
4.1	Gravitational well of the solar system . . . . .	52
4.2	Comet 67P/CG at 2.7 AU . . . . .	55
4.3	Comet 67P/CG at 2.35 AU . . . . .	56
4.4	Comet 67P/CG at 2.0 AU . . . . .	57
4.5	Comet 67P/CG at 1.65 AU . . . . .	58
4.6	Comet 67P/CG at 1.3 AU . . . . .	59
4.7	Global morphology for Ceres at 2.62 AU . . . . .	62
4.8	Magnetic field magnitude at Callisto . . . . .	66
4.9	Ion number density at Callisto . . . . .	67



## List of acronyms

3D	Three-dimensional
67P/CG	67P/Churyumov-Gerasimenko
ASC	Advanced Simulation and Computing
C3	Callisto 3 flyby by <i>Galileo</i>
C9	Callisto 9 flyby by <i>Galileo</i>
C10	Callisto 10 flyby by <i>Galileo</i>
C30	Callisto 30 flyby by <i>Galileo</i>
CFL	Courant-Friedrichs-Lewy
DOE	Department of Energy
ESA	European Space Agency
EUV	Extreme ultraviolet
JUICE	JUpiter ICy moons Explorer
MHD	Magnetohydrodynamics
NASA	National Aeronautics and Space Administration
NNSA	National Nuclear Security Administration
OASCR	Office of Science / Advanced Scientific Computing Research
ODE	Ordinary differential equation
PDE	Partial differential equation
PDS	Planetary Data System
PIC	Particle in cell
SRIM	Stopping and Range of Ions in Matter



# Sammanfattning

Här studerar jag “plasmaväxelverkan med isiga kroppar i solsystemet”, det vill säga, min strävan är att förstå de grundläggande processerna som styr sådana interaktioner. Genom att använda numerisk modellering i kombination med observationer på plats vid himlakropparna kan man förstå sig på deras interna strukturer och rymdmiljöer.

Efter en bred översikt över de fysiska lagar som styr ett rymdplasma följer en mer detaljerad del. Denna innehåller metoder för hur man kan modellera växelverkan mellan rymdplasma och isiga kroppar. Numerisk modellering av rymdplasma appliceras på de isiga himlakropparna Callisto (en måne kring Jupiter), dvärgplaneten Ceres (lokaliserad i asteroidbältet mellan Mars och Jupiter) och kometen 67P/Churyumov-Gerasimenko.

Det tidsvarierande magnetiska fältet kring Jupiter inducerar strömmar inuti den elektriskt ledande månen Callisto. Dessa strömmar skapar magnetfältsstörningar som tros vara relaterade till ett elektriskt ledande hav under Callistos yta. Plasmaflödet i närheten av Callisto påverkas i hög grad av dessa magnetfältsstörningar. Genom att använda en hybrid-plasma-lösare har växelverkan modellerats, där effekten av magnetisk induktion har inkluderats. Resultaten stämmer väl överens med magnetfältsdata från förbiflygningarna av Callisto (C3 och C9) som gjordes av den obemannade rymdfarkosten *Galileo* i dess bana kring Jupiter. Den magnetiska konfigurationen som uppstår möjliggör ett inflöde av laddade joner på Callistos baksida. Plasma som träffar ytan slår bort materia och skapar Callistos tunna atmosfär.

En långtidsstudie av solvindsprotoner sett från rymdfarkosten *Rosetta* utfördes då kometen 67P/Churyumov-Gerasimenko närmade sig solen. Ultraviolett strålning från solen joniserar det neutrala vattnet i kometens koma (kometens atmosfär). Nylikt joniserade vattenmolekyler plockas upp av solvindsflödet och tvingar solvindsprotonernas banor att böjas av, så att rörelsemängden bevaras. Denna effekt ökar stadigt då kometen närmar sig solen. Solvinden böjs av kraftigt, men förlorar inte mycket energi. Hybridmodellering av solvindens växelverkan bekräftar att kraften som verkar på solvinden till störst del får den att böjas av, medan kraften som verkar till att sänka dess fart är mycket lägre.

Ceres har enligt observationer av rymdteleskopet *Herschel* under 2012 och 2013 haft högt utflöde av vattenånga från dess yta. Där har två regioner identifierats som källor för vattenångan. Eftersom Ceres roterar kommer källornas regioner göra det också. Plasmaväxelverkan i närheten av Ceres beror i hög grad på vattenångskällans placeringen, medan det inte gör det långt ifrån Ceres. På global nivå har Ceres en kometliknande växelverkan med solvinden, där störningar i solvinden propagerar långt nedströms från Ceres.



We are not likely to know the right questions until we are close to knowing the answers.

---

Steven Weinberg

## CHAPTER 1

# Introduction

The continuously expanding ionized atmosphere of the Sun, the solar wind, is travelling at a supersonic speed radially outwards in our solar system. The solar wind is a highly ionized plasma, consisting mostly of protons and electrons. It carries with it a magnetic field which is frozen in to the particles' motion. As the solar wind flows through the solar system, it interacts with all obstacles in its way: planets, moons, comets and asteroids. Eventually, the solar wind reaches so far that it interacts with the plasma in-between stars, called the interstellar medium, at a distance of  $\sim 100$  astronomical units (AU), i.e. 100 times the average distance between the Sun and the Earth. This can be considered the approximate extent of the solar system.

Water, or  $\text{H}_2\text{O}$ , is the second most common molecule in the solar system, surpassed only by molecular hydrogen,  $\text{H}_2$ . In the early solar system, water and rock with various compositions formed solid bodies made of ice and rock, where bodies of higher ice content are found farther out in the solar system.

Icy bodies are present in almost all possible environments of our solar system. Some have direct interaction with the solar wind, both near to the Sun (comets and asteroids), and far from the Sun (Kuiper belt objects such as Pluto). Icy satellites around the gas giants interact with the magnetospheric plasma of their parent bodies, like the Galilean moons of Jupiter, Rhea and Enceladus around Saturn, the satellites of Uranus and Neptune's moon Triton.

The ambient plasma environment, and how the plasma interacts with the icy bodies, can best be measured by in situ observations. These measurements are paramount inputs when using numerical models of such physical systems. The internal structure of an icy body can be inferred by modelling how the plasma environment interacts with such a body, while at the same time comparing the results to observations.

This knowledge, combined with observations using spectroscopy, imaging, gravitational mapping, etc., all aim to reach the ultimate goal: to understand the origin and evolution of icy bodies. This is another jigsaw piece needed in order to explain the big puzzle of our solar system's past, present and future.

### 1.1 Modelling space plasmas

Space plasmas are often modelled as a magnetohydrodynamical (MHD) fluid. However, many observed physical phenomena cannot be captured by such models, e.g., a non-Maxwellian velocity distribution or finite gyroradius effects [20]. Therefore kinetic models are used, which can discretise the velocity space, making the problem six-dimensional. With a particle in cell (PIC) approach, the charge distributions of particles are represented as discrete particles, while the electromagnetic fields are stored on a spatial grid. Since the electric potential by each particle felt by their neighbours needs to be considered, the potential should not be Debye shielded, and thus the cell size should be smaller than the Debye length. This makes great computational demands, since the Debye length, e.g., in the solar wind, is around 10 m, as discussed in Section 2.1.1.

Many macroscopic problems in space plasma physics are characterized by an ion gyroradius comparable to the scale of the system. For these problems, a fluid description of the ions is inadequate. When the frequencies of interest are low compared to the ion cyclotron frequency, the effects of high-frequency phenomena, such as electromagnetic radiation and waves associated with electron inertia, are generally negligible [35]. For global interactions, e.g., between planets and the solar wind, a hybrid model is more adequate, where ions are represented as fully kinetic macroparticles and electrons as a fluid.

In order to model the plasma interaction with icy bodies, a thorough breakdown of the laws governing plasmas is needed; these are summarized in Chapter 2.

The hybrid solver used in the included papers has been developed by Holmström [20], and is since 2012 part of the open FLASH software developed by the Flash Center at the University of Chicago [13]. In Chapter 3 the general approximations and implementations of the hybrid code are presented, along with several useful techniques when dealing with numerical simulations.

The background to various icy bodies and their environments which have been investigated in the included papers are presented in Chapter 4.

The main conclusions of the included papers are summarized in Chapter 5.

The mathematician plays a game in which he himself invents the rules while the physicist plays a game in which the rules are provided by Nature, but as time goes on it becomes increasingly evident that the rules which the mathematician finds interesting are the same as those which Nature has chosen.

---

Paul Adrien Maurice Dirac

## CHAPTER 2

# Space plasma physics

This chapter presents a breakdown of the laws governing plasmas. This is the foundation needed in order to describe the dynamics of plasmas, which in turn are implemented in numerical plasma models to study the plasma interaction with icy bodies.

The chapter begins with a brief explanation of what defines a plasma. This is followed by charged particle dynamics, both single particle motion and when represented as collective distributions. In the end, more detailed representations are presented, including atmospheric (neutral) outflow from bodies, magnetic induction inside conductive bodies and waves in the plasma.

## 2.1 Definition of a plasma

Plasma is a fundamental state of matter, consisting of ionized gas. However, any ionized gas cannot be called a plasma, since there is always some small degree of ionization in any gas. A useful definition of a plasma:

*A plasma is a quasi-neutral gas of charged and neutral particles which exhibits collective behaviour [7].*

These conditions must be satisfied in a non-collisional plasma:

1. Quasi-neutrality (Debye shielding):  $\lambda_D \ll L$ ,  
where  $\lambda_D$  is the Debye length introduced in Section 2.1.1 and  $L$  is the typical length scale of a system.
2. Collective behaviour (free particles):  $\Lambda \gg 1$ ,  
where  $\Lambda$  is the plasma parameter, i.e. the amount of particles within a volume of

$\lambda_D^3$ , introduced in Section 2.1.2.

3. Non-collisional:  $\omega_{p,e} \tau_{n,e} \gg 1$ ,  
where the electron plasma frequency  $\omega_{p,e}$  and electron-neutral collisional frequency  $\tau_{n,e}$  are introduced in Section 2.1.3.

A more detailed description of these conditions is given in the following sections.

### 2.1.1 Debye shielding

For a plasma to be quasi-neutral, it must have about equal number of positive and negative charges per volume element [4]. Such a volume element needs to be large enough to contain a sufficient number of particles, yet be small compared to the characteristic lengths for variations of macroscopic parameters such as density and temperature. In each volume element, the microscopic fields of each individual charged particle must cancel each other out. Consider a plasma consisting of two charged species: ions with charge,  $q_i = Ze$  and electrons with charge,  $q_e = -e$ , where  $e$  is the elementary charge, and  $Z$  is an integer describing how many electrons have been stripped from a neutral atom/molecule, resulting in an ion. When considering a large enough volume element, the ambient plasma (electron) density is defined as:  $n_0 = n_e = Zn_i$ , where  $n_e$  is the electron density and  $n_i$  the ion density.

Consider a motionless ion in the plasma (denoted ‘t’). The electric Coulomb potential field,

$$\phi_C(r) = \frac{q_t}{4\pi\epsilon_0 r}, \quad (2.1)$$

of the ion will be partially compensated by particles of opposite sign in its vicinity, i.e. the electrons. Here  $\epsilon_0$  is the free space permittivity and  $r$  is the radial distance from the point charge.

Because electrons are highly mobile, they will accelerate toward the ion, pass it, and continue on. On average, this results in more electrons near the ion than at larger distances. In a region where the density is distorted, charge neutrality becomes violated and the resulting electric potential,  $\phi_D(r)$ , must satisfy Poisson’s equation,

$$\nabla^2 \phi_D(r) = -\frac{1}{\epsilon_0} \sum_s n_s q_s, \quad (2.2)$$

which is *Gauss’s law* for an electrostatic field (see Equation 2.22), and can in our case be written as

$$\nabla^2 \phi_D(r) = -\frac{e}{\epsilon_0} [Zn_i - n_e(r)]. \quad (2.3)$$

## 2.1. DEFINITION OF A PLASMA

The ion number density is unchanged,  $n_i = n_0/Z$ , while the electron number density,  $n_e(r)$ , will include the perturbation caused by the ion. If one assumes the electrons are Maxwellian distributed in velocity at constant temperature,  $T_e$ , the stationary *momentum density conservation equation* without convective derivatives is

$$0 = -\nabla p_e(r) - n_e(r) e \mathbf{E}, \quad (2.4)$$

where  $p_e$  is the electron scalar pressure and  $\mathbf{E}$  the electric field. Since this is electrostatic, the electric field is expressed as  $\mathbf{E} = -\nabla \phi_D$ . The pressure is  $p_e(r) = k_B T_e n_e(r)$ , where  $k_B$  is Boltzmann's constant. Rewriting Equation 2.4 yields

$$k_B T_e \nabla n_e(r) = e n_e(r) \nabla \phi_D(r). \quad (2.5)$$

The solution of this equation is called *Boltzmann's law* for the electron number density,

$$n_e(r) = n_0 \exp \left[ \frac{e \phi_D(r)}{k_B T_e} \right], \quad (2.6)$$

at equilibrium [4].

For weak potentials,  $e |\phi_D| \ll k_B T_e$ , Poisson's equation (Equation 2.3) takes the form

$$\nabla^2 \phi_D(r) = \frac{n_0 e^2}{\epsilon_0 k_B T_e} \phi_D(r) \quad (2.7)$$

when applying a Taylor expansion of first order to Equation 2.6.

Solving this differential equation with the condition that the distorted potential must look like the Coulomb potential in Equation 2.1 close to the ion, i.e.  $\phi_D(r) \rightarrow \phi_C(r)$  when  $r \rightarrow 0$ , the potential assumes the form

$$\phi_D(r) = \phi_C(r) \exp \left( -\frac{r}{\lambda_D} \right), \quad (2.8)$$

and becomes *Debye shielded* [4], where  $\lambda_D$  is the Debye length and equal to

$$\lambda_D = \left( \frac{\epsilon_0 k_B T_e}{n_0 e^2} \right)^{1/2}. \quad (2.9)$$

The Debye length is thus the typical screening distance of the electrostatic field made by an ion in a quasi-neutral plasma. In order for a plasma to be quasi-neutral, the physical dimension of the system,  $L$ , must be large compared to the Debye length, which gives the *first plasma criterion*:

$$\lambda_D \ll L. \quad (2.10)$$

## CHAPTER 2. SPACE PLASMA PHYSICS

---

This means that two regions of plasma separated by a distance,  $L$ , will appear neutral to each other if  $\lambda_D \ll L$ . On the scale of the Debye length, the motion of a single electron will be significantly affected by the individual potentials of all its neighbouring particles, while on average it follows the dynamics of macroscopic fields.

The screening of electron charges by the ions can be derived in a similar way [4]. By adding that potential into Poisson's equation (Equation 2.7), the effective Debye length becomes

$$\lambda_{D,\text{eff}}^{-2} = \lambda_D^{-2} + \lambda_{D,i}^{-2} \propto n_0 \left( \frac{1}{T_e} + \frac{Z}{T_i} \right), \quad (2.11)$$

where the ion Debye length is

$$\lambda_{D,i} = \left( \frac{\epsilon_0 k_B T_i}{Z n_0 e^2} \right)^{1/2}. \quad (2.12)$$

In hybrid simulation codes, which will be discussed in Chapter 3, quasi-neutrality is assumed. Therefore the smallest length scale of the system, the cell size, should be much larger than the Debye length to achieve a physical solution.

In the solar wind, accounting for only electrons and protons with number density  $n_0 = 5 \text{ cm}^{-3}$  at typical temperatures  $T_e = 1 \cdot 10^5 \text{ K}$  and  $T_i = 5 \cdot 10^4 \text{ K}$  [10], the Debye lengths are  $\lambda_D = 10 \text{ m}$  and  $\lambda_{D,i} = 7 \text{ m}$ . When studying plasma interactions with solar system bodies, the interesting length scales are usually at least of the order of kilometres.

In the Jovian magnetosphere at Callisto's orbit, assuming a plasma consisting of electrons and single-charged oxygen with number density  $n_0 = 0.15 \text{ cm}^{-3}$  and temperatures  $T_e = 5 \cdot 10^6 \text{ K}$  and  $T_i = 6 \cdot 10^5 \text{ K}$  [28], the corresponding Debye lengths are  $\lambda_D = 430 \text{ m}$  and  $\lambda_{D,i} = 150 \text{ m}$ . Compared to the size of Callisto, which has a radius of about 2410 km, the Debye lengths are small.

### 2.1.2 Plasma parameter

The sphere around the ion with a radius of the Debye length is called the *Debye sphere*. Since the shielding effect is the result of the collective behaviour inside a Debye sphere, it is necessary that this sphere contains sufficiently many charged particles. The number of electrons within this sphere is the *Debye number*,

$$N_D = \frac{4\pi}{3} n_0 \lambda_D^3 \propto T_e^{3/2} n_0^{-1/2}. \quad (2.13)$$

The term  $n_0 \lambda_D^3$  is often called the *plasma parameter*,  $\Lambda$ , which gives the *second plasma criterion*:

$$\Lambda \gg 1. \quad (2.14)$$

This quantifies what is meant by free particles, i.e. the assumption of weak potentials,  $e|\phi_D| \ll k_B T_e$  [4]. The mean inter-particle distance in the plasma is approximately  $\lambda_{ip} \approx n_0^{-1/3}$ . Rewriting Equation 2.14 with the definition of Debye length from Equation 2.9 yields

$$\Lambda^{2/3} = (4\pi)^{-1} \frac{k_B T_e}{e |\phi_D(\lambda_{ip})|} \exp\left(-\frac{\lambda_{ip}}{\lambda_D}\right) \gg 1. \quad (2.15)$$

If  $\Lambda \gg 1$  is valid, it follows that  $e|\phi_D| \ll k_B T_e$ .

A fully ionized plasma is non-collisional as long as the second plasma criterion is fulfilled [4].

In the solar wind at the orbit of Earth and in the Jovian magnetosphere at Callisto's orbit, the plasma parameter has approximate values of about  $\Lambda = 5 \cdot 10^9$  and  $\Lambda = 1 \cdot 10^{13}$  respectively, and thus satisfy the second plasma criterion.

### 2.1.3 Plasma frequency

Some plasmas, like the Earth's ionosphere, are not fully ionized [4]. If the charged particles collide too often with neutrals, they will be forced into equilibrium with the neutrals. Then the medium will no longer behave as a plasma, but rather as an electrically conducting neutral gas.

If the quasi-neutral plasma is locally perturbed by some external force or any other fluctuation, the highly mobile electrons will become accelerated and attempt to restore the charge balance. Due to their inertia they will move back and forth around their equilibrium position. By solving the electron fluid continuity equation with momentum conservation and applying Poisson's law for a small perturbation of electron density, the solution will result in what is called a *Langmuir oscillation*, given by the dispersion relation:

$$\omega^2 = \omega_{p,e}^2 \equiv \frac{n_0 e^2}{m_e \epsilon_0}, \quad (2.16)$$

where  $\omega_{p,e}$  is the (electron) plasma frequency, and  $m_e$  the electron mass. Here the electrons will perform an oscillation around the position of the ions.

For the electrons to be unaffected by collisions with neutrals, the average time between collisions,  $\tau_{n,e}$ , must be much larger than the reciprocal of the plasma frequency,

$$\omega_{p,e} \tau_{n,e} \gg 1. \quad (2.17)$$

This is the *third plasma criterion*.

In a lower frequency regime, ion inertia can no longer be neglected, and ion oscillations also become apparent. Their characteristic oscillation frequency is given by the dispersion relation:

$$\omega^2 = \omega_{p,i}^2 \equiv \frac{Zn_0 e^2}{m_i \epsilon_0}, \quad (2.18)$$

where  $\omega_{p,i}$  is the ion plasma frequency, and  $m_i$  the ion mass. For the plasma to be completely decoupled from the neutrals, the same criterion as in Equation 2.17 must apply to the ions as well,  $\omega_{p,i} \tau_{n,i} \gg 1$ .

In the intermediate range,  $\omega_{p,i} \tau_{n,i} \lesssim 1 \ll \omega_{p,e} \tau_{n,e}$ , the ions will couple to the neutrals while the electrons are free [4].

## 2.2 Single particle motion

Charged particles govern the evolution of electromagnetic fields, and the fields in turn determine the dynamics of the particles. This system has to be solved self-consistently. If, instead, the macroscopic electromagnetic fields are known for all points in space at all times, the dynamics of any particle can be solved. This is called *single particle motion*. In this section, the equation of motion is solved analytically for a plasma with homogeneous fields. This gives a very useful approximation for the plasma interaction with resistive, inert (plasma absorbing) solar system objects, e.g., the Moon, Dione and Rhea. In reality, the plasma affects the fields, but an approximation of homogeneous fields around an object is sometimes a good assumption. With this knowledge, macroscopic parameters such as number density and flux can be derived for any point in the plasma (most interestingly close to the surface of an object).

### 2.2.1 Field equations

We define a net space densities in charge,  $\rho$ , and current,  $\mathbf{J}$ ,

$$\rho = \sum_s n_s q_s, \quad (2.19)$$

$$\mathbf{J} = \sum_s n_s q_s \mathbf{v}_s, \quad (2.20)$$

where  $s$  denotes different charged species, and  $\mathbf{v}_s$  their velocities. Since charges and particles cannot be destroyed, we have the fundamental charge and current conservation equation,

$$\frac{\partial \rho}{\partial t} + \nabla \cdot \mathbf{J} = 0. \quad (2.21)$$



Charged particles at rest are the source of the electric field,  $\mathbf{E}$ . On the other hand, charged particles moving with a velocity are current elements generating a magnetic field,  $\mathbf{B}$  [4]. The field equations (*Maxwell's equations*) have the form:

$$\epsilon_0 \nabla \cdot \mathbf{E} = \rho, \quad (2.22)$$

$$\nabla \cdot \mathbf{B} = 0, \quad (2.23)$$

$$\nabla \times \mathbf{E} + \frac{\partial \mathbf{B}}{\partial t} = 0, \quad (2.24)$$

$$\frac{1}{\mu_0} \nabla \times \mathbf{B} - \epsilon_0 \frac{\partial \mathbf{E}}{\partial t} = \mathbf{J}. \quad (2.25)$$

In most space plasmas the displacement current,  $\partial \mathbf{E} / \partial t$ , can be neglected for low-frequency phenomena (magnetostatics) [10]. In a model without the transverse (divergence-free) part of the displacement current, no light waves are created, and is called the *Darwin approximation*, or the non-radiative limit [35, 20].

### 2.2.2 Equation of motion

The equation of motion for a test particle (denoted 't') of mass,  $m_t$ , and charge,  $q_t$ , where electromagnetic forces are dominating, i.e. the *Lorentz force*, can be written as

$$\dot{\mathbf{v}}_t = \frac{q_t}{m_t} (\mathbf{E} + \mathbf{v}_t \times \mathbf{B}), \quad (2.26)$$

where the velocity,  $\mathbf{v}_t(t)$ , is the time derivative of the position,  $\mathbf{r}_t(t)$ :

$$\dot{\mathbf{r}}_t = \mathbf{v}_t. \quad (2.27)$$

The motion of a charged particle is governed by the electromagnetic fields, which in turn are governed by the dynamics of the ensemble of charged particles. From a physical point of view, the macroscopic electric and magnetic fields are just representations of the average charge and current density distributions in space.

If the macroscopic fields are known for a system and constant in time, one can use so-called *test particles* to find the motion of any particle.

The change of energy of a particle can be achieved by taking the inner product of Equation 2.26 with  $\mathbf{v}$ , resulting in

$$\frac{d}{dt} \left( \frac{m_t v_t^2}{2} \right) = q_t (\mathbf{E} \cdot \mathbf{v}_t), \quad (2.28)$$

and noting that  $(\mathbf{v}_t \times \mathbf{B}) \cdot \mathbf{v}_t = 0$ . The energy of a charged particle can only change when a component of its velocity is along the electric field. Summing over all particles (ions and electrons) and averaging over volume gives us the equation

$$\frac{dW}{dt} = \mathbf{E} \cdot \mathbf{J}, \quad (2.29)$$

where  $W$  is the average energy of all particles per unit volume [4].

### 2.2.3 Analytical solution to the equation of motion

In the rest of this section, an analytical solution of the equation of motion is derived for homogeneous electromagnetic fields that are constant in time, and then applied by immersing a resistive inert body in the plasma and achieving the velocity distribution for any point on its surface. This can be used as an approximate but fast way of solving particle trajectories around a body in space, instead of self-consistently solving the equation of motion for particles and the field equations by other numerical methods.

The derivation of the Lorentz force is found in many textbooks, e.g., in *Baumjohann & Treumann*, 1996 [4]. There, the solution for the electric field and magnetic field are solved separately and later combined with a *Lorentz transformation*. In what follows, the derivation containing both fields is presented.

Consider a non-collisional plasma homogeneously distributed in space, of any velocity distribution, moving with a constant bulk velocity,  $\mathbf{u}$ , where the magnetic field,  $\mathbf{B}$ , and electric field,  $\mathbf{E}$ , are constant in time and space. The particles will behave as test particles and the equation of motion will only depend on the particles' own velocities,  $\mathbf{v}_t$ .

#### Coordinate system

Consider a right-handed coordinate system where the unit vectors are

$$\hat{\mathbf{z}} = \hat{\mathbf{x}} \times \hat{\mathbf{y}}. \quad (2.30)$$

The bulk velocity is set to

$$\mathbf{u} = u_x \hat{\mathbf{x}}. \quad (2.31)$$

Now, one can always find a coordinate system where

$$\mathbf{B} = B_x \hat{\mathbf{x}} + B_z \hat{\mathbf{z}}, \quad (2.32)$$

with its magnitude as  $B$ .

There are neither curls nor divergences of homogeneous fields. Since there are no density gradients or collisions either, the force acting on a particle moving with the bulk velocity,  $\mathbf{u}$ , is zero, i.e.  $\mathbf{E} + \mathbf{u} \times \mathbf{B} = 0$ , and the electric field is the *convective electric field* and given by

$$\mathbf{E} = -\mathbf{u} \times \mathbf{B}. \quad (2.33)$$

Note that  $\mathbf{E} = E_y \hat{\mathbf{y}}$ .

### Derivation

The equation of motion (Equation 2.26) can be written as

$$\dot{\mathbf{v}}_t = \frac{q_t}{m_t} [(\mathbf{v}_t - \mathbf{u}) \times \mathbf{B}], \quad (2.34)$$

where the dot,  $\dot{\phantom{x}}$ , represents the time derivative operator,  $d/dt$ . Now dropping the denotation of each test particle, and expanding Equation 2.34 into each coordinate:

$$\dot{v}_x = \frac{q}{m} [v_y B_z], \quad (2.35)$$

$$\dot{v}_y = \frac{q}{m} [v_z B_x - (v_x - u_x) B_z], \quad (2.36)$$

$$\dot{v}_z = \frac{q}{m} [-v_y B_x], \quad (2.37)$$

where only  $v_x$ ,  $v_y$ , and  $v_z$  depend on time. Taking the time derivative of Equation 2.36 gives

$$\ddot{v}_y = \frac{q}{m} [\dot{v}_z B_x - \dot{v}_x B_z], \quad (2.38)$$

which is simplified by using the expressions of  $\dot{v}_x$  and  $\dot{v}_z$  from Equations 2.35 and 2.37:

$$\ddot{v}_y = -\left(\frac{qB}{m}\right)^2 v_y. \quad (2.39)$$

Recognizing the characteristic gyrofrequency as  $\omega = |q|B/m$  [4] and solving Equation 2.39 yields

$$v_y = A_1 \cos \omega t + A_2 \sin \omega t, \quad (2.40)$$

where  $A_1$  and  $A_2$  are constants. After applying a time derivative we get

$$\dot{v}_y = A_2 \omega \cos \omega t - A_1 \omega \sin \omega t. \quad (2.41)$$

The values of  $A_1$  and  $A_2$  can be expressed as the initial values of the velocities (denoted '0'). Equation 2.40 at  $t = 0$  gives

$$A_1 = v_{y0}, \quad (2.42)$$

and combining Equations 2.36 and 2.41 yields

$$A_2 = \text{sign}(q) \frac{v_{z0} B_x - (v_{x0} - u_x) B_z}{B}, \quad (2.43)$$

where  $\text{sign}(q) = q/|q|$ .

Using the expression of  $v_y$  from Equation 2.40, one can solve the acceleration along each direction, in Equations 2.35, 2.36 and 2.37, resulting in:

$$\begin{aligned} \dot{v}_x = \text{sign}(q) \frac{B_z}{B} v_{y0} \omega \cos \omega t \\ + \left\{ \frac{B_x}{B^2} [v_{z0} B_z + (v_{x0} - u_x) B_x] - (v_{x0} - u_x) \right\} \omega \sin \omega t, \end{aligned} \quad (2.44)$$

$$\begin{aligned} \dot{v}_y = \text{sign}(q) \frac{v_{z0} B_x - (v_{x0} - u_x) B_z}{B} \omega \cos \omega t \\ - v_{y0} \omega \sin \omega t, \end{aligned} \quad (2.45)$$

$$\begin{aligned} \dot{v}_z = -\text{sign}(q) \frac{B_x}{B} v_{y0} \omega \cos \omega t \\ + \left\{ \frac{B_z}{B^2} [v_{z0} B_z + (v_{x0} - u_x) B_x] - v_{z0} \right\} \omega \sin \omega t. \end{aligned} \quad (2.46)$$

Now, integrating each component of acceleration,  $\dot{v}$ , to get the velocity,  $v$ :

$$\begin{aligned} v_x = u_x + \frac{B_x}{B^2} [v_{z0} B_z + (v_{x0} - u_x) B_x] \\ + \left\{ (v_{x0} - u_x) - \frac{B_x}{B^2} [v_{z0} B_z + (v_{x0} - u_x) B_x] \right\} \cos \omega t \\ + \text{sign}(q) \frac{B_z}{B} v_{y0} \sin \omega t, \end{aligned} \quad (2.47)$$

$$\begin{aligned} v_y = v_{y0} \cos \omega t \\ + \text{sign}(q) \frac{v_{z0} B_x - (v_{x0} - u_x) B_z}{B} \sin \omega t, \end{aligned} \quad (2.48)$$

$$\begin{aligned} v_z = \frac{B_z}{B^2} [v_{z0} B_z + (v_{x0} - u_x) B_x] \\ + \left\{ v_{z0} - \frac{B_z}{B^2} [v_{z0} B_z + (v_{x0} - u_x) B_x] \right\} \cos \omega t \\ - \text{sign}(q) \frac{B_x}{B} v_{y0} \sin \omega t, \end{aligned} \quad (2.49)$$

and another integration for the position,  $\mathbf{r} = (x, y, z)$ :

$$\begin{aligned} x = x_0 + \text{sign}(q) \frac{v_{y0} B_z}{\omega B} + \left\{ u_x + \frac{B_x}{B^2} [v_{z0} B_z + (v_{x0} - u_x) B_x] \right\} t \\ - \text{sign}(q) \frac{v_{y0} B_z}{\omega B} \cos \omega t \\ + \left\{ (v_{x0} - u_x) - \frac{B_x}{B^2} [v_{z0} B_z + (v_{x0} - u_x) B_x] \right\} \frac{1}{\omega} \sin \omega t, \end{aligned} \quad (2.50)$$

$$\begin{aligned} y = y_0 + \text{sign}(q) \frac{v_{z0} B_x - (v_{x0} - u_x) B_z}{\omega B} \\ - \text{sign}(q) \frac{v_{z0} B_x - (v_{x0} - u_x) B_z}{\omega B} \cos \omega t + \frac{v_{y0}}{\omega} \sin \omega t, \end{aligned} \quad (2.51)$$

$$\begin{aligned} z = z_0 - \text{sign}(q) \frac{v_{y0} B_x}{\omega B} + \left\{ \frac{B_z}{B^2} [v_{z0} B_z + (v_{x0} - u_x) B_x] \right\} t \\ + \text{sign}(q) \frac{v_{y0} B_x}{\omega B} \cos \omega t \\ + \left\{ v_{z0} - \frac{B_z}{B^2} [v_{z0} B_z + (v_{x0} - u_x) B_x] \right\} \frac{1}{\omega} \sin \omega t. \end{aligned} \quad (2.52)$$

When averaging acceleration/velocity/position over a gyroperiod,  $t_g = 2\pi/\omega$ , this results in the dynamics of the gyrocentre of the particle. Let us use the notation that an average over a gyroperiod of a quantity,  $p$ , is

$$\langle p \rangle = \frac{1}{t_g} \int_{t-t_g/2}^{t+t_g/2} p dt. \quad (2.53)$$

Note that  $\langle \cos \omega t \rangle = \langle \sin \omega t \rangle = 0$ , and  $\langle t \rangle = t$ . The solution for the gyrocentre's position,  $\langle \mathbf{r} \rangle$ , becomes:

$$\langle x \rangle = x_0 + \text{sign}(q) \frac{v_{y0} B_z}{\omega B} + \left\{ u_x + \frac{B_x}{B^2} [v_{z0} B_z + (v_{x0} - u_x) B_x] \right\} t, \quad (2.54)$$

$$\langle y \rangle = y_0 + \text{sign}(q) \frac{v_{z0} B_x - (v_{x0} - u_x) B_z}{\omega B}, \quad (2.55)$$

$$\langle z \rangle = z_0 - \text{sign}(q) \frac{v_{y0} B_x}{\omega B} + \left\{ \frac{B_z}{B^2} [v_{z0} B_z + (v_{x0} - u_x) B_x] \right\} t, \quad (2.56)$$

and taking the time derivative to get the gyrocentre velocity:

$$\langle v_x \rangle = u_x + \frac{B_x}{B^2} [v_{z0} B_z + (v_{x0} - u_x) B_x], \quad (2.57)$$

$$\langle v_y \rangle = 0, \quad (2.58)$$

$$\langle v_z \rangle = \frac{B_z}{B^2} [v_{z0} B_z + (v_{x0} - u_x) B_x]. \quad (2.59)$$

Note that the gyrocentre's velocity is constant, and is zero in the direction of  $y$ , which is the direction of the convective electric field. Since  $\mathbf{E} \cdot \langle \mathbf{v} \rangle = 0$  (see Equation 2.28), the energy of a single particle might oscillate, but will on average stay the same. The position of the particle from Equations 2.50, 2.51 and 2.52 can now be simplified to:

$$x = \langle x \rangle_0 + \langle v_x \rangle t + (x_0 - \langle x \rangle_0) \cos \omega t + \frac{v_{x0} - \langle v_x \rangle}{\omega} \sin \omega t, \quad (2.60)$$

$$y = \langle y \rangle_0 + \langle v_y \rangle t + (y_0 - \langle y \rangle_0) \cos \omega t + \frac{v_{y0} - \langle v_y \rangle}{\omega} \sin \omega t, \quad (2.61)$$

$$z = \langle z \rangle_0 + \langle v_z \rangle t + (z_0 - \langle z \rangle_0) \cos \omega t + \frac{v_{z0} - \langle v_z \rangle}{\omega} \sin \omega t, \quad (2.62)$$

or in vector form,

$$\mathbf{r} = \langle \mathbf{r} \rangle_0 + \langle \mathbf{v} \rangle t + (\mathbf{r}_0 - \langle \mathbf{r} \rangle_0) \cos \omega t + \frac{\mathbf{v}_0 - \langle \mathbf{v} \rangle}{\omega} \sin \omega t, \quad (2.63)$$

where the two first terms represent the gyrocentre's motion, and the other terms represent the gyration around the gyrocentre. Now, the position for a particle at any time,  $t$ , is known if given its initial position and velocity, and constant homogeneous electromagnetic fields.

It can be shown that the two magnitudes  $|\mathbf{r}_0 - \langle \mathbf{r} \rangle_0|$ , and  $|\mathbf{v}_0 - \langle \mathbf{v} \rangle|/\omega$ , are the same and can be recognized as the gyroradius, also called the *Larmor radius* [4],  $r_g$ , and given by the expression:

$$\omega^2 r_g^2 = |(\mathbf{v}_0 - \mathbf{u})_\perp|^2 = v_{y0}^2 + \left[ \frac{v_{z0} B_x - (v_{x0} - u_x) B_z}{B} \right]^2. \quad (2.64)$$

Furthermore the two vectors are orthogonal to each other,  $(\mathbf{r}_0 - \langle \mathbf{r} \rangle_0) \cdot (\mathbf{v}_0 - \langle \mathbf{v} \rangle) = 0$ , with an acceleration always pointing towards the gyrocentre,  $\mathbf{a} = \omega^2 (\langle \mathbf{r} \rangle_0 - \mathbf{r}_0)$  for  $t = 0$ . In the frame of a particle's gyrocentre, it is *always* making a circular motion.

## Drifts

When looking at the average drifts of particles, consider the velocity of the gyrocentre from Equations 2.57, 2.58 and 2.59. The gyrocentre velocity along a magnetic field line is

given by

$$\langle \mathbf{v} \rangle_{\parallel} = \frac{\langle \mathbf{v} \rangle \cdot \mathbf{B}}{B^2} \mathbf{B}, \quad (2.65)$$

which equals

$$\langle \mathbf{v} \rangle_{\parallel} = \frac{v_{z0} B_x B_z + v_{x0} B_x^2}{B^2} \hat{\mathbf{x}} + \frac{v_{z0} B_z^2 + v_{x0} B_x B_z}{B^2} \hat{\mathbf{z}}, \quad (2.66)$$

where

$$|\langle \mathbf{v} \rangle_{\parallel}| = \frac{|v_{x0} B_x + v_{z0} B_z|}{B}, \quad (2.67)$$

and is completely independent of the bulk velocity,  $\mathbf{u}$ , and thus also the electric field,  $\mathbf{E}$ . The drift perpendicular to  $\mathbf{B}$  is then

$$\langle \mathbf{v} \rangle_{\perp} = \langle \mathbf{v} \rangle - \langle \mathbf{v} \rangle_{\parallel}, \quad (2.68)$$

which equals

$$\langle \mathbf{v} \rangle_{\perp} = \frac{u_x B_z^2}{B^2} \hat{\mathbf{x}} - \frac{u_x B_x B_z}{B^2} \hat{\mathbf{z}}, \quad (2.69)$$

where

$$|\langle \mathbf{v} \rangle_{\perp}| = \frac{|u_x B_z|}{B}, \quad (2.70)$$

and is completely independent of the initial conditions of the particle.

The parallel drift is simply the initial velocity along the magnetic field lines for a single particle, which does not change since no force is acting on it. The perpendicular drift is the *E-cross-B drift* given by  $\langle \mathbf{v} \rangle_{\perp} = \mathbf{E} \times \mathbf{B} / B^2$ , and is a collective drift which is the same for all particles. Note that a particle with initial velocity equal to the bulk velocity,  $\mathbf{v}_0 = \mathbf{u}$ , has the expected drift,  $\langle \mathbf{v} \rangle = \mathbf{v} = \mathbf{v}_0 = \mathbf{u}$ .

## Application

The analytical solution of the equation of motion for a plasma with homogeneous electromagnetic fields constant in time can be used to achieve an approximation of the velocity distribution at any point on the surface of a body immersed in such a plasma.

Similar analytical approaches have been done for solar system bodies, e.g., the Moon by Hutchinson [23, 24, 25].

Consider a highly resistive, inert, spherical object of radius,  $R$ , immersed in this plasma. Let origo be at the centre of the object. The equation for a particle's position (Equation 2.63) can be used to solve the motion of any particle. Now it is possible to know the macroscopic moments at the surface of the object, such as number density and precipitating flux. When given an ambient velocity distribution (see Section 2.3), one can

backtrack all possible velocities of the distribution,  $\mathbf{v}_0$ , where time,  $t = 0$ , represents when the particles are at the surface. If the position of a particle is ever inside the object,  $|\mathbf{r}| < R$ , during its last gyroperiod,  $-2\pi/\omega \leq t < 0$ , that part of the velocity distribution is removed for that position on the surface.

Since the surface is assumed to be inert (plasma absorbing), no particle should originate from the surface. Consider an infinitesimal backtracking in time at  $t = 0$  by Taylor expanding  $\mathbf{r}$ . For a particle to come from a valid origin, three conditions arise:

1. The radial velocity should be negative (going into the surface),

$$\mathbf{v}_0 \cdot \mathbf{r}_0 < 0. \quad (2.71)$$

2. If the radial velocity is tangential to the surface or zero,  $\mathbf{v}_0 \cdot \mathbf{r}_0 = 0$ , the radial acceleration has to be positive,

$$\dot{\mathbf{v}}_0 \cdot \mathbf{r}_0 > 0. \quad (2.72)$$

3. If the radial velocity and acceleration are initially tangential or zero,  $\mathbf{v}_0 \cdot \mathbf{r}_0 = 0$  and  $\dot{\mathbf{v}}_0 \cdot \mathbf{r}_0 = 0$ , then:

$$\ddot{\mathbf{v}}_0 \cdot \mathbf{r}_0 \leq 0. \quad (2.73)$$

There is no point for higher derivatives, since they will be a constant times a two order lower derivative, e.g.,  $\ddot{\mathbf{v}}_0 = -\omega^2 \mathbf{v}_0$ .

The solution for  $|\mathbf{r}| < R$  is not analytically solvable in general for  $t < 0$ . However, if the gyroradius is extremely small compared to the object,  $r_g \ll R$  for all  $\mathbf{v}_0$ , one can approximate the position of the particle with the gyrocentre,  $\mathbf{r} \approx \langle \mathbf{r} \rangle$ . For a particle to come from a valid origin, the three conditions in Equations 2.71, 2.72 and 2.73 reduce to the criterion:

4. The gyrocentre radial velocity should be negative at  $t = 0$ ,

$$\langle \mathbf{v} \rangle \cdot \mathbf{r}_0 \leq 0, \quad (2.74)$$

which is the only criterion needed if  $r_g \ll R$ .

This might be useful when considering electrons, since they often have a much smaller gyroradius than ions.

For an arbitrary gyroradius, however, a numerically effective algorithm can be implemented using  $n$  phases,  $\alpha_n = \omega t_n$ , in the range  $-2\pi \leq \alpha_n < 0$ . The least numerically expensive is to choose  $n$  equally spaced phases in the given range. We get the criterion:



5. The solutions for the distance to the centre must be positive,

$$r_n^2 > R^2, \quad (2.75)$$

for all  $n$ , where  $\mathbf{r}_n = \mathbf{r}(t_n)$ .

That a particle comes from a valid origin,  $|\mathbf{r}| > R$ , is checked for each phase, of all velocities of the velocity distribution, for all positions on the surface of the object, and if it does not: that part of the velocity distribution is removed for that point on the surface.

In total, five criteria have been presented. Depending on the problem, different ones should be used. For a problem where  $r_g \ll R$ , only criterion 4 needs to be fulfilled. Otherwise criteria 1, 2, 3 and 5 need to be fulfilled.

### Testing the algorithm

Consider the moon Callisto, immersed in the Jovian magnetospheric plasma. With plasma parameters from previous studies of Callisto [34], we can summarize the plasma parameters as seen in Table 2.1, and use the algorithm described previously in this section. Assume that the plasma consists of oxygen ions,  $O^+$ , at thermodynamic equilibrium. The distribution of velocities will be a Maxwellian velocity distribution (discussed in detail in the next section). The net flux of  $O^+$  is given by  $\Gamma_0 = n_0 u_0$ , where  $n_0$  is the ambient ion number density and  $u_0$  is the ambient ion bulk speed.

**Table 2.1:** Table of parameters for the plasma environment of Callisto.

Parameter	Notation	Unit	Value
Ion number density	$n_0$	$[\text{cm}^{-3}]$	1.1
Ion temperature	$T_i$	$[\text{eV}]$	200
External magnetic field	$\mathbf{B}_0$	$[\text{nT}]$	(0, 0, -35)
$O^+$ cyclotron frequency	$\omega$	$[\text{rad/s}]$	0.21
Plasma bulk velocity	$\mathbf{u}_0$	$[\text{km/s}]$	(-175, 0, 0)
$O^+$ thermal velocity	$v_{\text{th}}$	$[\text{km/s}]$	49
$O^+$ gyroradius for $v = v_{\text{th}}$	$r_g$	$[\text{km}]$	233
Callisto's radius	$R$	$[\text{km}]$	2410

Assuming that the electromagnetic field are constant, the number density and precipitating flux of oxygen ions at Callisto's surface looks like the surface maps in Figure 2.1.

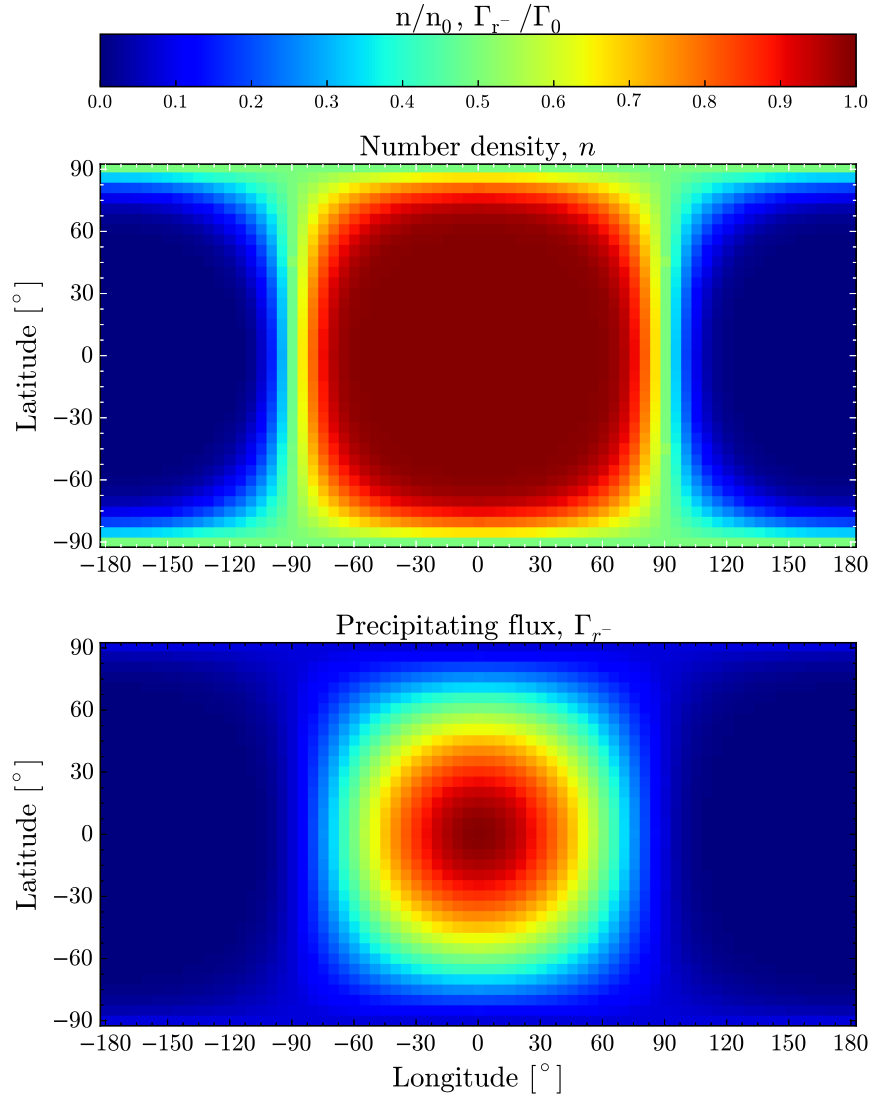


**Figure 2.1:** The number density and the precipitating flux of  $O^+$  at Callisto's surface, plotted on a mesh of the surface, where  $(0^\circ \text{ longitude}, 0^\circ \text{ latitude})$  corresponds to the point where the bulk of the magnetospheric plasma hits the surface from zenith. There, the magnetic field is pointing downwards, and the electric field to the right.

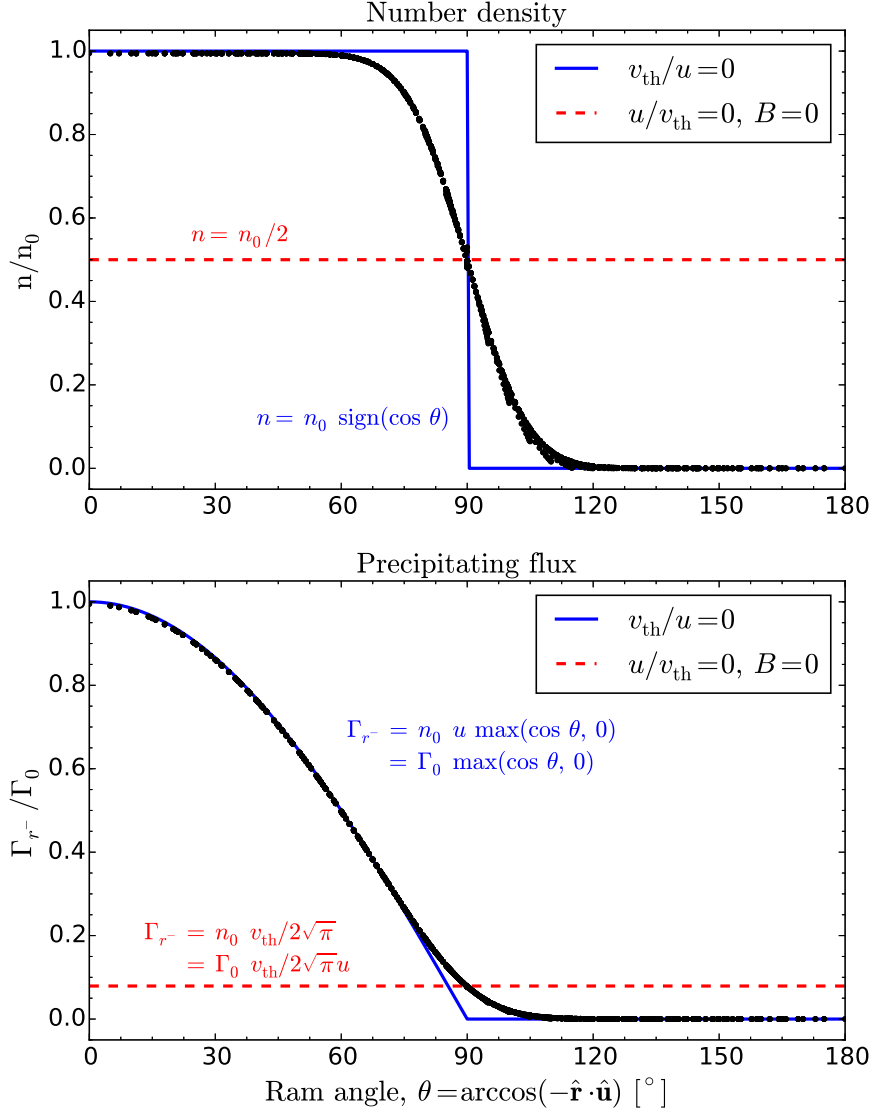


**Figure 2.2:** The number density and the precipitating flux of  $O^+$  at Callisto's surface, plotted against the ram angle,  $\theta = \arccos(-\hat{\mathbf{r}} \cdot \hat{\mathbf{u}})$ . Each black dot corresponds to a value on Callisto's surface. The blue line corresponds to the extreme case when the thermal velocity is much less than the bulk speed,  $v_{th}/u \ll 1$ , while the red dashed line corresponds to the extreme case of an unmagnetised plasma with a thermal velocity much higher than the bulk speed of the magnetospheric plasma,  $B = 0$  and  $v_{th}/u \gg 1$ .

Figure 2.2 shows the oxygen ion number density and precipitating flux dependences on the ram angle,  $\theta = \arccos(-\hat{\mathbf{r}} \cdot \hat{\mathbf{u}})$ , which is the angle between the nadir direction ( $-\hat{\mathbf{r}}$ ) and the bulk velocity  $\mathbf{u}$ . As black dots, the central grid values from Figure 2.1 are plotted. Coloured lines are drawn, corresponding to the extremes: if the thermal velocity was zero (blue solid line) and if the bulk velocity and magnetic field magnitude were zero (red dashed line).

The interaction is quite symmetric in the ram angle, since the thermal gyroradius,  $r_g$ , is only about 1/10 of Callisto's radius.

The algorithm demonstrated takes around 20 s (wall clock time) to initiate, run and plot. It is useful as a first view of the different length scales and time scales involved in the plasma interaction of a body.

## 2.3 Velocity space distribution

In this section, a whole set of particles are described by their positions and velocities. By doing this, one may express the dynamics and characteristics of a collective plasma instead of following each particle's motion. This is achieved by expressing the set of particles as a distribution in both velocity and space.

The so-called *velocity space distribution function*,  $f(\mathbf{r}, \mathbf{v}, t)$ , is an averaged quantity of the phase space  $(\mathbf{r}, \mathbf{v})$  density, i.e. how many particles that exist within a phase space volume element,  $d\mathbf{r}d\mathbf{v}$ , at a certain time,  $t$ , for arbitrary positions and velocities [4].

If one integrates the distribution over all velocities, one gets the number density of the particles,

$$n(\mathbf{r}, t) = \int_{-\infty}^{\infty} \int_{-\infty}^{\infty} \int_{-\infty}^{\infty} f(\mathbf{r}, \mathbf{v}, t) dv_x dv_y dv_z, \quad (2.76)$$

where the normalized distribution function can be expressed as

$$\hat{f}(\mathbf{r}, \mathbf{v}, t) = \frac{f(\mathbf{r}, \mathbf{v}, t)}{n(\mathbf{r}, t)}. \quad (2.77)$$

### 2.3.1 Macroscopic quantities

The physical macroscopic quantities such as number density,  $n$ , bulk velocity,  $\mathbf{u}$ , average temperature,  $T$ , etc., do not depend on a single particle's velocity but only on position and time. The mean of any microscopic quantity, such as the velocity of particles,  $\mathbf{v}$ , is given

## 2.3. VELOCITY SPACE DISTRIBUTION

by the expression:

$$\langle \mathbf{v} \rangle(\mathbf{r}, t) = \int_{-\infty}^{\infty} \int_{-\infty}^{\infty} \int_{-\infty}^{\infty} \mathbf{v} \hat{f}(\mathbf{r}, \mathbf{v}, t) dv_x dv_y dv_z. \quad (2.78)$$

The mean, or *bulk velocity*,  $\mathbf{u}$ , is defined as:

$$\mathbf{u}(\mathbf{r}, t) = \langle \mathbf{v} \rangle. \quad (2.79)$$

The mean flux of particles in, e.g., the  $x$ -direction,  $\Gamma_x$ , is then

$$\Gamma_x = n \langle v_x \rangle. \quad (2.80)$$

The *pressure tensor* is defined as the contribution due to the fluctuation of the velocities of particles around the bulk velocity, and is given by

$$\mathbf{P}(\mathbf{r}, t) = mn \langle (\mathbf{v} - \mathbf{u})^2 \rangle, \quad (2.81)$$

where  $m$  is the mass of a single particle [4]. The *temperature tensor*,  $\mathbf{T}$ , is related to the pressure tensor as

$$\mathbf{P} = nk_B \mathbf{T}. \quad (2.82)$$

In an isotropic plasma, the traceless (off-diagonal) parts of  $\mathbf{P}$  and  $\mathbf{T}$  vanish, and what is left is only the scalar pressure,  $p$ , defined as:

$$p(\mathbf{r}, t) = \frac{mn}{3} \langle |\mathbf{v} - \mathbf{u}|^2 \rangle, \quad (2.83)$$

where the *kinetic temperature*,  $T$ , is given by  $p = nk_B T$ . The kinetic temperature can be calculated for *any* distribution function, and does not necessarily need to be a *true* temperature in a thermodynamic sense, which can only be calculated for plasmas in or close to thermal equilibrium.

### 2.3.2 Maxwellian distribution

The velocity space distribution of a collisionless plasma in thermodynamic equilibrium is the *Maxwellian velocity distribution*, or simply Maxwellian. Thermal equilibrium implies that there are no energy exchange processes in the plasma (no free energy). The particles are distributed randomly around the average velocity, i.e. the bulk velocity,  $\mathbf{u}$ . In a homogeneous and isotropic plasma at thermal equilibrium, the distribution is independent of position and time, and takes the form

$$f(\mathbf{v}) = \frac{n}{(\sqrt{\pi} v_{th})^3} \exp \left( -\frac{|\mathbf{v} - \mathbf{u}|^2}{v_{th}^2} \right), \quad (2.84)$$

where the thermal velocity is defined as  $v_{\text{th}} = (2k_B T/m)^{1/2}$ , and  $T$  is the temperature of the plasma. A Maxwellian is often used as an approximation for plasmas encountered in our solar system (discussed in Chapter 4).

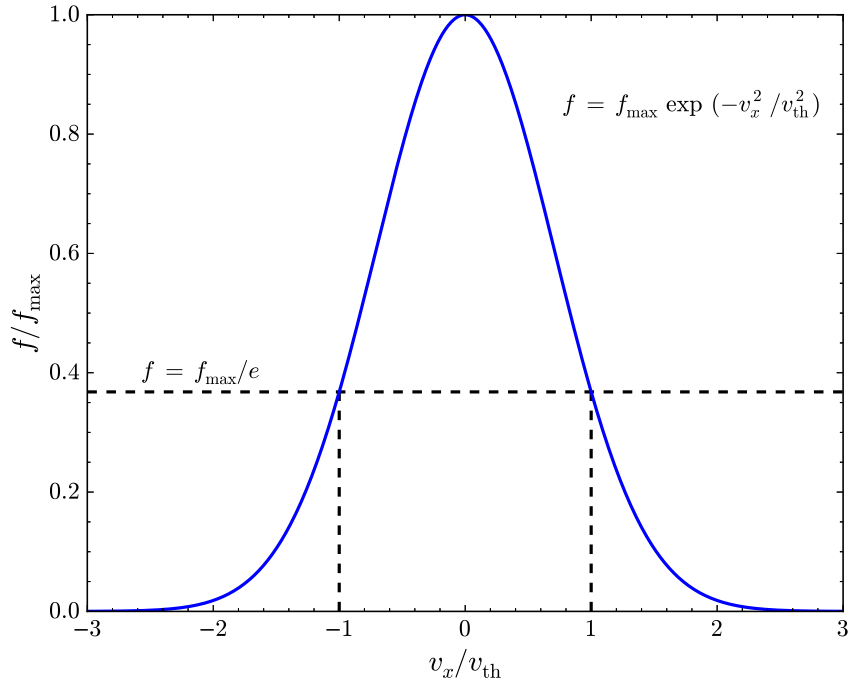


**Figure 2.3:** A non-drifting Maxwellian velocity distribution function,  $f$ , normalized to its maximum value at  $v_x = 0$ ,  $f_{\text{max}} = n/(\sqrt{\pi} v_{\text{th}})^3$ , in one dimension. The points at which the black dashed lines meet are where the distribution function amplitude has dropped to a value  $f_{\text{max}}/e$ , at  $|v_x| = v_{\text{th}}$ .

A *non-drifting* Maxwellian velocity distribution ( $u = 0$ ) is shown for one dimension ( $x$ ) in Figure 2.3. An example of a discretised Maxwellian velocity distribution, used to characterise the ambient plasma in the application of the previous section (Section 2.2.3), is shown in Figure 2.4, where the bulk velocity is assumed to be only in the  $x$ -direction,  $\mathbf{u} = u_x \hat{\mathbf{x}}$ .

### 2.3. VELOCITY SPACE DISTRIBUTION

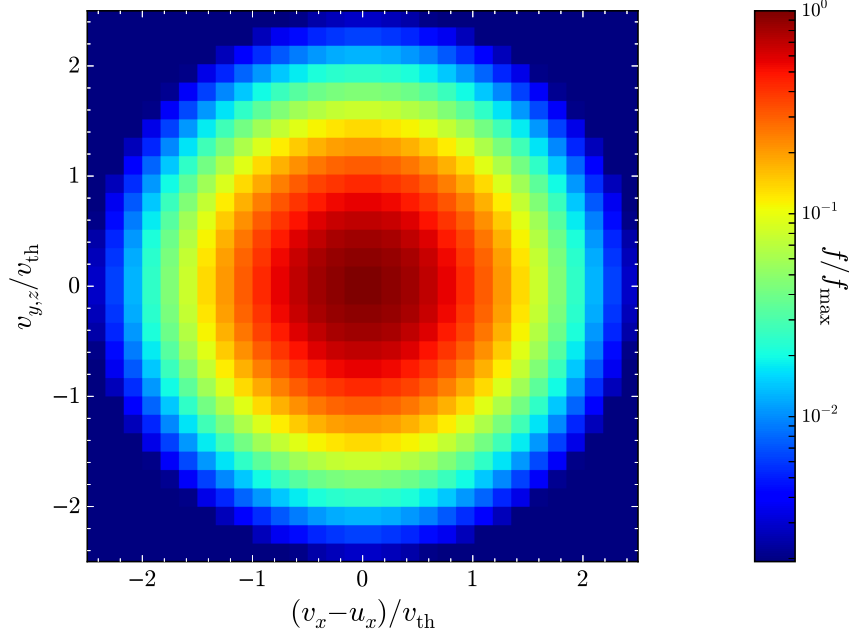


**Figure 2.4:** A discretised Maxwellian velocity distribution function,  $f$ , normalized to its maximum value at  $\mathbf{v} = \mathbf{u} = u_x \hat{\mathbf{x}}$ ,  $f_{\max} = n/(\sqrt{\pi} v_{\text{th}})^3$ .

When not considering the whole velocity distribution but only parts of it, the mean value of a quantity in this velocity domain takes the more general form:

$$\langle \mathbf{v} \rangle = \frac{\int_{v_z^{\min}}^{v_z^{\max}} \int_{v_y^{\min}}^{v_y^{\max}} \int_{v_x^{\min}}^{v_x^{\max}} \mathbf{v} f(\mathbf{v}) dv_x dv_y dv_z}{\int_{v_z^{\min}}^{v_z^{\max}} \int_{v_y^{\min}}^{v_y^{\max}} \int_{v_x^{\min}}^{v_x^{\max}} f(\mathbf{v}) dv_x dv_y dv_z}. \quad (2.85)$$

Consider a flat imaginary plane with a normal,  $\hat{\mathbf{N}}$ , where two orthonormal base vectors  $\hat{\perp}_1$  and  $\hat{\perp}_2$  lie in the plane. Let the angle between the bulk velocity and the normal of the plane be given by  $\theta$ . Now the bulk velocity can be written as

$$u_N = u \cos \theta, \quad (2.86)$$

$$u_{\perp_1} = u \sin \theta, \quad (2.87)$$

$$u_{\perp_2} = 0. \quad (2.88)$$

The flux magnitude through such a surface from one side to the other in the direction of  $\hat{\mathbf{N}}$  is given by

$$\Gamma_{N^+} = \int_0^\infty \int_{-\infty}^\infty \int_{-\infty}^\infty v_N f(\mathbf{v}) dv_{\perp_2} dv_{\perp_1} dv_N, \quad (2.89)$$

which can be expanded to

$$\begin{aligned}\Gamma_{N^+} = & \frac{n}{(\sqrt{\pi} v_{th})^3} \int_{-\infty}^{\infty} \exp \left[ -\frac{v_{\perp 2}^2}{v_{th}^2} \right] dv_{\perp 2} \\ & \int_{-\infty}^{\infty} \exp \left[ -\frac{(v_{\perp 1} - u \sin \theta)^2}{v_{th}^2} \right] dv_{\perp 1} \\ & \int_0^{\infty} v_N \exp \left[ -\frac{(v_N - u \cos \theta)^2}{v_{th}^2} \right] dv_N,\end{aligned}\quad (2.90)$$

The first two integrals both have the value  $\sqrt{\pi} v_{th}$ , and the last integral can be solved with a variable substitution,  $t = (v_N - u \cos \theta) / v_{th}$ , which results in the flux

$$\Gamma_{N^+} = n \left\{ u \cos \theta \left[ \frac{1 + \operatorname{erf} \left( \frac{u \cos \theta}{v_{th}} \right)}{2} \right] + \frac{v_{th}}{2\sqrt{\pi}} \exp \left[ -\frac{(u \cos \theta)^2}{v_{th}^2} \right] \right\}. \quad (2.91)$$

The part of the distribution which is going through the surface is given by

$$\begin{aligned}n_{N^+} &= \int_0^{\infty} \int_{-\infty}^{\infty} \int_{-\infty}^{\infty} f(\mathbf{v}) dv_{\perp 2} dv_{\perp 1} dv_N \\ &= n \left[ \frac{1 + \operatorname{erf} \left( \frac{u \cos \theta}{v_{th}} \right)}{2} \right].\end{aligned}\quad (2.92)$$

The mean speed through the surface along  $\hat{\mathbf{N}}$  is then

$$\begin{aligned}\langle v_{N^+} \rangle &= \frac{\Gamma_{N^+}}{n_{N^+}} \\ &= u \cos \theta + \frac{v_{th}}{\sqrt{\pi}} \left[ 1 + \operatorname{erf} \left( \frac{u \cos \theta}{v_{th}} \right) \right]^{-1} \exp \left[ -\frac{(u \cos \theta)^2}{v_{th}^2} \right].\end{aligned}\quad (2.93)$$

Note that for a zero bulk velocity, or  $\theta = 90^\circ$ , the flux through the surface is completely thermal and is called *random flux* [7],

$$\Gamma_{\text{random}} = \frac{n v_{th}}{2\sqrt{\pi}}. \quad (2.94)$$

Taking the net flux through the surface will cancel all thermal contributions and one gets the result:

$$\begin{aligned}\Gamma_N &= \Gamma_{N^+} - \Gamma_{N^-} \\ &= n u \cos \theta.\end{aligned}\quad (2.95)$$



### 2.3.3 Neutral non-collisional outflow

Consider an object in space which has a source of neutrals on its surface, creating a non-collisional atmosphere (exosphere) or a non-collisional plume. The total production rate of neutrals,  $Q$ , at the exobase (bottom of the exosphere) can then be expressed as

$$Q = \int \Gamma_{r+} dA, \quad (2.96)$$

where  $\hat{r}$  is the radial component from the centre of the object, and  $dA$  an area segment.

If one knows both the production rate, source area and the Maxwellian distribution at the exobase, it is possible to deduce the shape of the exosphere at all heights. This is interesting in itself, but also when considering the possible ionization that the exosphere can go through.

If neutrals are released into space from an object of negligible gravity with total production rate,  $Q$ , at time  $t = 0$ , the number of neutrals,  $N_n$ , will follow the differential equation

$$\frac{dN_n}{dt} = Q - v_d N_n, \quad (2.97)$$

where  $v_d$  is the destruction rate of neutrals, with destruction meaning all processes that change the fundamental structure of the molecule, either by dissociation, recombination or ionization. The solution of the total number of neutrals is

$$N_n(t) = \frac{Q}{v_d} [1 - \exp(-v_d t)]. \quad (2.98)$$

The total ion production rate,  $Q_i$ , becomes

$$\begin{aligned} Q_i(t) &= \frac{dN_i}{dt} = v_i N_n \\ &= \frac{v_i}{v_d} Q [1 - \exp(-v_d t)], \end{aligned} \quad (2.99)$$

where  $v_i$  is the ionization rate of neutrals and  $N_i$  the total number of ions.

The steady-state values are

$$N_n(\infty) = \frac{Q}{v_d}, \quad (2.100)$$

$$Q_i(\infty) = \frac{v_i}{v_d} Q. \quad (2.101)$$

The probability that a single neutral particle will ionize within a time,  $\Delta t$ , can be derived by solving the above equations for  $Q = 0$ , which results in

$$P_{n \rightarrow i}(\Delta t) = \frac{N_i(t + \Delta t) - N_i(t)}{N_n(t)} = \frac{v_i}{v_d} [1 - \exp(-v_d \Delta t)]. \quad (2.102)$$

For the case  $v_d \Delta t \ll 1$ , the probability can be written as

$$P_{n \rightarrow i}(\Delta t) \approx v_i \Delta t. \quad (2.103)$$

### Isotropic outflow

For an object such as a comet with radius,  $R$ , and negligible mass, assume an homogeneously distributed, isotropic production of, e.g., water vapour. The total flux of water vapour through any spherical shell around the object at distance  $r$  will be constant. This is called the Haser model [18]. Above the surface of the body ( $r > R$ ), the total flux of neutrals through a spherical shell is

$$\begin{aligned} Q &= A(r) \Gamma_{r+}(r) \\ &= 4\pi r^2 \langle v_{r+} \rangle n(r), \end{aligned} \quad (2.104)$$

where  $n(r) = n_{r+}$  is the number density and  $\langle v_{r+} \rangle$  is the mean velocity of water vapour in the radial direction, which is represented by Equation 2.93 for  $\theta = 0$  at the exobase, because the neutrals might be collisional close to the surface. The number density of water becomes

$$n(r) = \frac{Q}{4\pi r^2 \langle v_{r+} \rangle}. \quad (2.105)$$

Note that as soon as the neutrals become non-collisional, they will no longer have a Maxwellian distribution as they continue into space [49], since without any collisions or external forces all particles will eventually only have a radial velocity component.

Furthermore, if one accounts for losses, the flux will decrease exponentially with time, where the time is measured as the mean time since the neutrals left the surface, i.e.  $t = (r - R) / \langle v_{r+} \rangle$ . The number density becomes

$$n(r) = \frac{Q}{4\pi r^2 \langle v_{r+} \rangle} \exp \left[ -\frac{v_d (r - R)}{\langle v_{r+} \rangle} \right], \quad (2.106)$$

where  $v_d$  is the destruction rate of water vapour. The ion production rate becomes

$$q_i(r) = v_i n(r), \quad (2.107)$$

with  $v_i$  as the water ionization rate.

It is possible to get an analytical solution of the number density of neutrals for an isotropic exosphere which is Maxwellian distributed at the exobase, when including gravity [49].

### Localized sources

Often, production of neutrals are not isotropic in nature, but localized to source regions on a planetary surface, and gravity can not be neglected. When an analytical solution cannot be found for the number density of neutrals at all points, it is useful to use test particles instead.

When non-collisional neutrals at the surface of a source region with area,  $A$ , are homogeneously created with a total production rate of  $Q$ , the neutrals can be launched in a model according to any velocity distribution. Then, for each time step,  $\Delta t$ , the probability that particles ionize/destruct is checked, and the particles are changed accordingly.

Assuming a Maxwellian distribution for the neutrals with some temperature,  $T$ , and bulk velocity  $\mathbf{u}$ , the number density of the *full* Maxwellian distribution at the exobase,  $n$ , is related to the production rate as

$$n = \frac{Q}{A \langle v_{r+} \rangle} \left[ \frac{2}{1 + \operatorname{erf} \left( \frac{u \cos \theta}{v_{\text{th}}} \right)} \right], \quad (2.108)$$

where  $\theta$  is the angle between the bulk velocity and the radial direction.

## 2.4 Magnetic induction

The Jovian moons Europa and Callisto both have conducting regions under their crusts, thought to be subsurface oceans [27, 30, 53, 34]. This section gives the laws governing magnetic induction applied to such bodies by an external time-varying magnetic field.

Consider a spherical body of radius,  $R$ , with some conductivity,  $\sigma(r)$ , immersed in a plasma. According to Ampère's law (Equation 2.25), any curl of the magnetic field is represented by a current. This current can in principle be generated by an external change in the magnetic field,  $\partial \mathbf{B} / \partial t$ , by Faraday's law, or by the convective electric field generated by the plasma itself.

### 2.4.1 Time-varying magnetic field

Let the body be immersed in a stationary plasma with a time-varying magnetic field. The fundamental equation to describe the induction process in a solid body with electrical

## CHAPTER 2. SPACE PLASMA PHYSICS

---

conductivity,  $\sigma(r)$ , is Faraday's law (Equation 2.24), where the electric field is given by  $\mathbf{E} = \mathbf{J}/\sigma$ , and the displacement current,  $\partial\mathbf{E}/\partial t$ , is neglected,

$$\frac{\partial\mathbf{B}}{\partial t} = -\nabla \times \mathbf{E} = -\nabla \times \left( \frac{1}{\sigma\mu_0} \nabla \times \mathbf{B} \right). \quad (2.109)$$

A simple representation is a conducting shell inside the body with isotropic conductivity,  $\sigma_0$ . Let  $r_1$  represent the inner boundary of the shell, and  $r_0$  the outer boundary. Assuming zero conductivity in the core and the outermost shell gives a conductivity profile with radial distance:

$$\sigma(r) = \begin{cases} 0, & \text{for } r < r_1, \\ \sigma_0, & \text{for } r_1 < r < r_0, \\ 0, & \text{for } r_0 < r < R. \end{cases} \quad (2.110)$$

Let the external magnetic field be spatially homogeneous, with one part which is independent of time,  $\mathbf{b}_0$ , and one which is not (called the primary field),  $\mathbf{B}_0$ , that has a temporal variation expressed by a frequency  $\omega_B$ . The induced field (or secondary field) from the body is  $\mathbf{B}_1$ , and the total magnetic field can be expressed as

$$\mathbf{B}(t) = \mathbf{b}_0 + \mathbf{B}_0(t) + \mathbf{B}_1(t). \quad (2.111)$$

Faraday's law (Equation 2.109) for a infinitely conducting body ( $\sigma_0 \rightarrow \infty$ ,  $r_0 = R$ ) can be solved [48] and the currents induced by the primary field can be represented by the secondary field,

$$\mathbf{B}_1^\infty(t) = \frac{\mu_0}{4\pi r^5} \{ 3[\mathbf{r} \cdot \mathbf{M}^\infty(t)] \mathbf{r} - r^2 \mathbf{M}^\infty(t) \}, \quad (2.112)$$

for  $r > R$ , with  $\mathbf{M}$  as the magnetic moment,

$$\mathbf{M}^\infty(t) = -\frac{4\pi R^3 \mathbf{B}_0(t)}{\mu_0}. \quad (2.113)$$

For the case of a finite conductivity, the secondary field will be weaker than the primary field and its phase lags, but no more than a quarter of a period. The steady-state solution can be related to the perfectly conducting sphere by

$$\mathbf{B}_1(t) = A \mathbf{B}_1^\infty \left( t + \frac{\Phi}{\omega} \right), \quad (2.114)$$

where  $A < (r_0/R)^3$  and  $-\pi/2 \leq \Phi < 0$  [48]. This solution is valid as long as  $\omega_B \ll \sigma_0 \mu_0 c^2$ , with  $c$  as the speed of light in vacuum, and if the primary field can be expressed as a potential field, i.e. if  $\nabla \times \mathbf{B} = \mu_0 \mathbf{J} = 0$  for  $r > r_0$  [48]. The currents in the plasma must therefore be zero for the above equation to hold, and the conductivity large enough with respect to the frequency,  $\omega_B$ .

By dimensional analysis of Equation 2.109, the typical diffusion time,  $\tau_D$ , on a length scale of  $L$  is

$$\tau_D = \sigma_0 \mu_0 L^2, \quad (2.115)$$

where the frequency-dependent skin depth,  $\delta$ , can be expressed as

$$\delta(\omega_B) = \left( \frac{2}{\omega_B \sigma_0 \mu_0} \right)^{1/2}, \quad (2.116)$$

which is the typical width of the current layer of the conductive shell [48].

If the skin depth is small compared to the thickness of the shell,

$$\delta \lesssim r_0 - r_1, \quad (2.117)$$

the shell is considered *conductive*.

For a geometry often seen in planetary magnetospheres, where the primary field is perpendicular to the flow of plasma (whose effect is neglected), the magnetic field magnitude is increased both in front and in the wake of the body [30, 53, 48].

### 2.4.2 Plasma-induced currents

Let the body be immersed in a moving plasma, where the external magnetic field is constant in time ( $\omega_B = 0$ ). Let the body have the same conductivity profile as in Equation 2.110. The electric field can be expressed as

$$\mathbf{E} = -\mathbf{u} \times \mathbf{B} + \frac{\mathbf{J}}{\sigma}. \quad (2.118)$$

Faraday's law can now be written as

$$\frac{\partial \mathbf{B}}{\partial t} = \nabla \times (\mathbf{u} \times \mathbf{B}) - \nabla \times \left( \frac{1}{\sigma \mu_0} \nabla \times \mathbf{B} \right), \quad (2.119)$$

with the first term being the *convective term*, and the second the *diffusive term*. The system at steady state without wave propagation will be electrostatic,  $\partial \mathbf{B} / \partial t = 0$ .

The electric field in the highly conductive undisturbed plasma is only the convective term (the field is frozen in to the plasma), while inside the body there is no plasma so the electric field is only given by the diffusive term. A current in the direction of the convective electric field,  $-\mathbf{u} \times \mathbf{B}$ , is induced in the body to balance the electric field.

Dimensional analysis gives the typical skin depth,  $\delta$ , to which extent the magnetic field penetrates into the conducting body,

$$\delta(u) = \frac{2}{u \sigma_0 \mu_0}. \quad (2.120)$$

For  $\delta \gg r_0 - r_1$ , the current will be almost homogeneously distributed in the body, but the current will be extremely small, making the magnetic field easily diffuse through the object; thus the object can be considered as *resistive*. If  $\delta \lesssim r_0 - r_1$ , however, the current will travel within a thin layer under the conducting surface of thickness  $\sim \delta$ , and can be considered as *conductive*.

In general, the magnetic field lines will drape around the object, and the geometry will lead to a compression of magnetic field lines in front of the body (the ram side), and a relaxation of the magnetic field in the wake of the body [28, 47].

## 2.5 Ion waves

A wave is a perturbation of the electromagnetic fields of the plasma and can be classified by being either electrostatic ( $\partial \mathbf{B}_1 / \partial t = 0$ ) or electromagnetic ( $\partial \mathbf{B}_1 / \partial t \neq 0$ ), where  $\mathbf{B}_1$  is the perturbation of the magnetic field around its mean value over time,  $\mathbf{B}_0$ . The total magnetic field is given by

$$\mathbf{B}(t) = \mathbf{B}_0 + \mathbf{B}_1(t), \quad (2.121)$$

where  $B_1 \ll B_0$ , for linear wave phenomena.

### 2.5.1 Electrostatic waves

In many space plasmas, the flow is supersonic, i.e. the typical bulk flow of plasma is faster than the average thermal velocities. This is represented by the sonic Mach number,  $M_S$ , which can be expressed as

$$M_S = \frac{u}{v_S}, \quad (2.122)$$

being greater than 1 for a supersonic plasma [4], where

$$v_S = \frac{\sum_s \gamma_s p_s}{\sum_s n_s m_s}, \quad (2.123)$$

is the speed of sound, or thermal variations, and  $\gamma_s$  is the adiabatic index of each species, which is related to the number of degrees of freedom,  $N_s$ , by:

$$\gamma_s = \frac{2 + N_s}{N_s}. \quad (2.124)$$

For a plasma consisting of one ion species, and by neglecting the mass of the electron, the speed of sound can be simplified to

$$v_s = \frac{k_B (Z \gamma_e T_e + \gamma_i T_i)}{m_i}, \quad (2.125)$$

where  $Z$  represents the charge of a single ion in terms of the elementary charge,  $e$ .

In the low-frequency regime, a sound wave propagating along the magnetic field is an *ion acoustic wave* where ions suffer a one-dimensional compression (along the perturbed electric field), thus having only one degree of freedom, giving,  $\gamma_i = 3$ . The electrons move so fast relative to these waves that they have time to equalize their temperature everywhere: therefore, the electrons are isothermal and  $\gamma_e = 1$  [7]. Thus, the sound speed is not strictly constant, but will have a weak dependence on the frequency of the wave itself, since  $\gamma_s(\omega)$ .

The general morphology of all atmosphereless bodies immersed in a flowing plasma is that there will be a significant wake of particles downstream of the body. This is seen for bodies (discussed more in Chapter 4) in both the solar wind, such as the Moon [22], and in magnetospheric plasmas, such as Callisto orbiting Jupiter [34].

## 2.5.2 Electromagnetic waves

What differs greatly in different plasmas of the solar system is the speed at which magnetic perturbations can propagate (discussed further in Chapter 4). A perturbation along the magnetic field caused by ions is called an *Alfvén wave* [7], and has in the low-frequency regime the wave speed:

$$v_A = \frac{B}{(\mu_0 \sum_s n_s m_s)^{1/2}}, \quad (2.126)$$

which for one ion species can be simplified to

$$v_A = \frac{B}{(\mu_0 m_i n_e / Z)^{1/2}}, \quad (2.127)$$

where the corresponding Alfvénic Mach number is

$$M_A = \frac{u}{v_A}. \quad (2.128)$$

The wave propagating perpendicular to the magnetic field lines is called a *magnetosonic wave*, and has in the low-frequency regime the wave speed

$$v_{MS} = (v_s^2 + v_A^2)^{1/2}, \quad (2.129)$$

with its corresponding magnetosonic Mach number

$$M_{\text{MS}} = \frac{u}{v_{\text{MS}}}. \quad (2.130)$$

In the limit of an unmagnetised plasma,  $B \rightarrow 0$ , the magnetosonic wave turns into an ion acoustic wave.



## CHAPTER 3

# Hybrid modelling of plasmas

In a hybrid model, ions are represented as fully kinetic macroparticles and electrons as a fluid.

The hybrid solver has been developed by Holmström [20], and is since 2012 part of the open FLASH software developed by the Flash Center at the University of Chicago [13].

In what follows, the general approximations and implementations of the hybrid code are presented, along with several useful techniques when dealing with numerical simulations.

### 3.1 Hybrid approximations

Due to the fluid nature of electrons, a hybrid model is applicable to length and time scales of ions. When neglecting these small-scale structures, and high-frequency phenomena, some useful approximations can be made.

Most hybrid solvers have the following approximations [20]:

1. Quasi-neutrality. The total charge density,  $\rho$ , is zero

$$\rho = \sum_s \rho_s = \rho_e + \sum_I \rho_I = 0, \quad (3.1)$$

where  $I$  denotes all ion species. The electron charge density can be written as

$$\rho_e = - \sum_I \rho_I. \quad (3.2)$$

2. Ampère's law without the transverse displacement current (also called the Darwin approximation) provides the total current density

$$\mathbf{J} = \frac{1}{\mu_0} \nabla \times \mathbf{B}, \quad (3.3)$$

where the electron current density can be found as

$$\mathbf{J}_e = \mathbf{J} - \sum_I \mathbf{J}_I. \quad (3.4)$$

Quasi-neutrality implies that the electron velocity,  $\mathbf{u}_e$ , can be written as

$$\mathbf{u}_e = \frac{\mathbf{J}_e}{\rho_e} = \frac{-\mathbf{J} + \sum_I \mathbf{J}_I}{\sum_I \rho_I}. \quad (3.5)$$

3. Massless electrons,  $m_e = 0$  for the inertial term, lead to the electron momentum equation

$$m_e \frac{d(n_e \mathbf{u}_e)}{dt} = 0 = \rho_e \mathbf{E} + \mathbf{J}_e \times \mathbf{B} - \nabla \cdot \mathbf{P}_e + \mathcal{C}_e, \quad (3.6)$$

where  $\mathcal{C}_e$  is a force term due to collisions between an electron and any type of particle or electron-wave interactions, and  $\mathbf{P}_e$  is the electron pressure tensor.

This provides an equation of state (Ohm's law) for the electric field:

$$\mathbf{E} = \frac{1}{\sum_I \rho_I} \left[ \left( \mathbf{J} - \sum_I \mathbf{J}_I \right) \times \mathbf{B} - \nabla \cdot \mathbf{P}_e + \mathcal{C}_e \right]. \quad (3.7)$$

The electric field contains no unknowns, and can thus be calculated at all times.

4. The electron pressure is isotropic

$$\nabla \cdot \mathbf{P}_e = \nabla p_e, \quad (3.8)$$

and polytropic

$$\frac{\nabla p_e}{p_e} = \gamma_e \frac{\nabla \rho_e}{\rho_e}, \quad (3.9)$$

where  $\gamma_e$  is the polytropic index of electrons, as a free parameter. This results in

$$p_e \propto \rho_e^{\gamma_e}. \quad (3.10)$$

The polytropic index is often chosen as adiabatic, corresponding to Equation 2.124.

5. Faraday's law is used to advance the magnetic field in time,

$$\frac{\partial \mathbf{B}}{\partial t} = -\nabla \times \mathbf{E}. \quad (3.11)$$

Note that the gradient of electron pressure does not affect the evolution of the magnetic field, as can be seen by the vector identity  $\nabla \times \nabla p_e = 0$  in Faraday's law.

### 3.2 Hybrid equations

By the approximations from the previous section, it is possible to describe the evolution in time for the unknowns of the model: the particles' positions,  $\mathbf{r}_i$ , their velocities,  $\mathbf{v}_i$ , and the discrete magnetic field,  $\mathbf{B}_j$ . The ions are fully kinetic, and the magnetic field is stored in the centre of cubic cells on a discrete grid, where  $j$  denotes that a quantity is discretised in the centre of a grid cell.

Let the term,  $\mathcal{C}_e$ , represent electron collisions (with either ions or neutrals) where the target's momentum change is zero [4],

$$\mathcal{C}_e = -\rho_e \eta \mathbf{J}, \quad (3.12)$$

where  $\eta = 1/\sigma$ , is the resistivity of the medium.

The time advance of the unknowns can be written as a set of ordinary differential equations (ODEs) and a partial differential equation (PDE), that after discretisation become:

$$\frac{d\mathbf{r}_i}{dt} = \mathbf{v}_i, \quad (3.13)$$

$$\frac{d\mathbf{v}_i}{dt} = \frac{q_i}{m_i} \left[ \mathbf{E} + \mathbf{v}_i \times \mathbf{B} - \frac{\eta}{\mu_0} (\nabla \times \mathbf{B}) \right] + \frac{\mathbf{F}_{\text{ext}}}{m_i}, \quad (3.14)$$

$$\frac{\partial \mathbf{B}_j}{\partial t} = -\nabla_j \times \mathbf{E}_j, \quad (3.15)$$

where ' $\nabla_j \times$ ' is a discrete curl operator, using a central difference scheme,  $\mathbf{F}_{\text{ext}}$  is an external force such as gravity and the electric field is given by

$$\begin{aligned} \mathbf{E}_j = \frac{1}{\sum_I \rho_I} \left[ -\sum_I \mathbf{J}_I \times \mathbf{B}_j + \frac{1}{\mu_0} (\nabla_j \times \mathbf{B}_j) \times \mathbf{B}_j - \nabla_j p_e \right] \\ + \frac{\eta}{\mu_0} (\nabla_j \times \mathbf{B}_j). \end{aligned} \quad (3.16)$$

The electromagnetic fields experienced by each particle in the Lorentz force of Equation 3.14 are achieved by interpolating the fields between cell centres to the position of each particle.

The centre of mass for collisions between like particles will remain constant [7], and will thus give rise to very little diffusion and so is not considered here. Note that the resistive term in the electric field cancels out in the Lorentz force for ions.

The algorithm for advancing the ODEs and the PDE in time is an explicit cyclic leapfrog method using central differences [20, 38].

### 3.3 Resistivity

If collisions of any kind occur in a plasma, electrons will have more difficulty carrying a current through the medium, giving rise to a collective resistance represented by the resistivity,  $\eta$  [Ohm m].

The resistivity of a plasma where electrons move with respect to either neutrals or ions can be expressed as

$$\eta = \frac{m_e v_c}{n_e e^2}, \quad (3.17)$$

where  $v_c$  is the collisional frequency [4].

#### 3.3.1 Coulomb collisions

For a fully ionized plasma, collisions are due to Coulomb scattering between electrons and ions, and the Coulomb collision frequency [4] may be used (not discussed further here). This results in the *Spitzer resistivity*,

$$\eta_s = \frac{1}{16\pi \epsilon_0 \omega_{p,e}} \frac{\ln \Lambda}{\Lambda}, \quad (3.18)$$

where  $\Lambda$  is given by

$$\Lambda = \frac{4\pi}{Z} n_e \lambda_D^3, \quad (3.19)$$

for a plasma consisting of electrons and one ion species with charge,  $Ze$ . This  $\Lambda$  is within a factor  $4\pi/Z$  equal to the plasma parameter introduced in Equation 2.14. The term  $\ln \Lambda$  is called the *Coulomb logarithm* and has a value around 20 for space plasmas [10]. The Spitzer resistivity is in fact independent of the plasma density (except for the very weak dependence in  $\ln \Lambda$  for large  $\Lambda$ ). In practice, the proportionality is

$$\eta_s \propto T_e^{-3/2}. \quad (3.20)$$

In the solar wind at 1 AU, this resistivity is extremely small,  $\sim 10^{-5}$  Ohm m, and as such the plasma is extremely conducting. For all practical use, the resistivity of the plasma can be neglected. However, it can be set as nonzero in the model as a smoothing technique for the magnetic field (see Section 3.5).

#### 3.3.2 Implementation

A numerical problem occurs for low plasma densities in the electric field, since it tends towards infinity. A self-consistent, physically correct way of handling vacuum regions

is to express the electric field as  $\mathbf{E} = \eta \mathbf{J}$ , where  $\eta \rightarrow \infty$  [19]. This can be handled as setting the factor  $(\sum_I \rho_I)^{-1} = 0$  when  $\sum_I \rho_I < \rho_{\min}$ , with  $\rho_{\min}$  chosen arbitrarily as the condition for vacuum or being inside a body. For a spherical body of radius  $R$ , immersed in a plasma, one can use a radial resistivity profile  $\eta(r)$ , where  $\eta(r < R)$  represents the resistivity inside the body, and  $\eta(r > R)$  the resistivity outside the body.

In the hybrid model, the collisional term of the electric field cancels out in the Lorentz force, because there is no momentum transfer from the massless electrons, and thus no direct effect on the dynamics of the ions [1]. For advancing the magnetic field in Faraday's law, however, the collisional term plays a role. Note that the resistivity of the plasma can be set to a nonzero value in Faraday's law, and thus acts as a diffusive term. In this way, the plasma resistivity can be used as a tool to diffuse numerical oscillations in the magnetic field of the plasma. The resistivity of vacuum,  $\eta_v$ , is always set as high as possible.

In vacuum regions or inside an obstacle, Faraday's law becomes

$$\frac{\partial \mathbf{B}}{\partial t} = -\nabla \times \left( \frac{\eta}{\mu_0} \nabla \times \mathbf{B} \right), \quad (3.21)$$

as also seen in Equation 2.109 for magnetic induction [21].

#### Numerical scheme

For a numerical scheme of the electric field [21]: If the charge density is too low,  $\sum_I \rho_I < \rho_{\min}$ , and if located outside the body,  $r > R$ , it is considered as vacuum:  $(\sum_I \rho_I)^{-1} \mapsto 0$  and  $\eta = \eta_v$ . If inside the body,  $r \leq R$ , the plasma density is zero and the resistivity equal to the given profile:  $(\sum_I \rho_I)^{-1} \mapsto 0$  and  $\eta = \eta(r)$ . Finally, if outside the body,  $r > R$ , and the charge density is above the minimum limit,  $\sum_I \rho_I \geq \rho_{\min}$ , then it is considered as plasma and the resistivity is equal to the given profile:  $\eta = \eta(r)$ . To summarize:

$$\eta = \begin{cases} \eta_v & \text{if } r > R \text{ and } \sum_I \rho_I < \rho_{\min}, \\ \eta(r) & \text{otherwise.} \end{cases} \quad (3.22)$$

The vacuum resistivity,  $\eta_v$ , should nominally be set to infinity, but this would mean an infinitely fast diffusion and is not practically possible for a simulation. This is addressed in the coming section.

### 3.4 Time step constraints

A model using finite differences will become inaccurate, or even unstable (for explicit solvers) if information is travelling more than one cell for every time step of the simulation. The constraints on the maximum time step allowed in a simulation are given by the Courant-Friedrichs-Lewy (CFL) conditions [9].

In the simulation domain of the hybrid model the discrete cells are cubic with their sides of lengths,  $\Delta x = \Delta y = \Delta z$ . Since the fields are calculated in the centre of each cell, diffusion, oscillations and propagation of particles and waves all have to be resolved within one time step of the simulation,  $\Delta t$ .

The general CFL condition for a propagation in a three-dimensional space of an explicit solver is

$$\Delta t < \left( \frac{|v_x|}{\Delta x} + \frac{|v_y|}{\Delta y} + \frac{|v_z|}{\Delta z} \right)^{-1}. \quad (3.23)$$

#### 3.4.1 Waves

The CFL condition for any wave or oscillation with frequency  $\omega$ , becomes

$$\Delta t < \frac{k \Delta x}{\sqrt{3} \omega}, \quad (3.24)$$

where  $k$  is the wave number [44]. To resolve the fastest wave with phase speed  $v_{ph} = \omega/k$ , the equation takes the form

$$\Delta t < \frac{\Delta x}{\sqrt{3} v_{ph}}. \quad (3.25)$$

#### 3.4.2 Oscillations

For the fastest oscillation with frequency  $\omega_{max}$ , the time step needs to resolve the biggest wave number on the grid,  $k_{max} = \pi/\Delta x$ , giving the constraint,

$$\Delta t < \frac{\pi}{\sqrt{3} \omega_{max}}, \quad (3.26)$$

which is completely independent of the cell size and will thus be the restriction for the time step at large cell sizes.

### 3.4.3 Particles

The propagation of a collection of particles needs to be resolved with the condition

$$\Delta t < \frac{\Delta x}{\max(\langle v_{x+} \rangle, \langle v_{x-} \rangle) + \max(\langle v_{y+} \rangle, \langle v_{y-} \rangle) + \max(\langle v_{z+} \rangle, \langle v_{z-} \rangle)}, \quad (3.27)$$

where the mean of a speed  $\langle v_{x+} \rangle$  for a Maxwellian distribution is calculated as in Equation 2.93, which for an arbitrary direction of the bulk velocity,  $\mathbf{u}$ , gets the maximum for  $\cos \theta = 1/\sqrt{3}$  in all directions, giving the constraint,

$$\Delta t < \frac{\Delta x}{\sqrt{3} u + \frac{3 v_{th}}{\sqrt{\pi}} \left[ 1 + \operatorname{erf} \left( \frac{u}{\sqrt{3} v_{th}} \right) \right]^{-1} \exp \left[ -\frac{u^2}{3 v_{th}^2} \right]}. \quad (3.28)$$

If the simulation also includes other types of particles that are not from a Maxwellian distribution, their movement also has to satisfy Equation 3.23.

Pick-up ions, for instance, will move at a maximum speed  $2|\mathbf{E} \times \mathbf{B}|/B^2$ , and thus for arbitrary direction of the E-cross-B drift on the grid have to satisfy

$$\Delta t < \frac{B^2 \Delta x}{2\sqrt{3} |\mathbf{E} \times \mathbf{B}|}. \quad (3.29)$$

### 3.4.4 Diffusion

The diffusion equation for the magnetic field advancement in time in Faraday's law (Equation 3.21) is similar to the heat equation and gives a time step for stability of

$$\Delta t < \frac{\mu_0 \Delta x^2}{2\eta}, \quad (3.30)$$

which will dominate the condition on the time step for high resistivities and small cell sizes, because of its square-dependence [21]. This condition is the dominant one for almost all modelled cases of the papers included in this thesis.

### 3.4.5 Massless electrons

The Hall term in Ohm's law ( $\mathbf{J} \times \mathbf{B}$ ) is associated with whistler dynamics. The whistler wave spectrum is cut off at the electron cyclotron frequency, but due to the assumption of massless electrons it is unbounded for the hybrid equations, and the frequency of

the wave,  $\omega$ , scales like  $\omega/\omega_{c,i} = (kc/\omega_{p,i})^2$  for large wave numbers,  $k$  [44]. Here  $\omega_{c,i}$  is the ion cyclotron frequency introduced in Equation 2.40, and  $\omega_{p,i}$  the ion plasma frequency introduced in Equation 2.18. This gives the time step constraint for three spatial dimensions

$$\Delta t < \frac{1}{\sqrt{3}\pi\omega_{c,i}} \left( \frac{\Delta x}{\delta_i} \right)^2 \propto \frac{q_i n_i}{B} \Delta x^2, \quad (3.31)$$

where  $\delta_i$  is the ion inertial length (the ion skin depth),  $\delta_i = c/\omega_{p,i} = v_A/\omega_{c,i}$ , with  $v_A$  as the Alfvén wave speed introduced in Equation 2.126.

### 3.4.6 Gravity

When it comes to neutrals, when neglecting collisions, the dominant force is the gravitational force, which gives the acceleration of a particle,

$$\mathbf{a} = \frac{\mathbf{F}_{\text{ext}}}{m} = -\frac{GM}{r^2} \hat{\mathbf{r}}, \quad (3.32)$$

where  $G$  is the gravitational constant, and  $M$  the mass of a massive body at a distance,  $r$ , where the unit vector  $\hat{\mathbf{r}}$  is pointing from the centre of the massive object.

For a particle in such a field which does not depend on the particle's motion and is not averaged at the centre of a grid cell, but given an analytical solution, it is not necessary for stability to satisfy the time step constraint in Equation 3.27. However, it is required in order to have particle statistics for each cell.

Instead, for numerical accuracy, the gravitational field needs to be resolved, namely:

$$\Delta t < \frac{|a_r|}{|\dot{a}_r|}, \quad (3.33)$$

which for a collection of Maxwellian distributed particles, calculated from the maximum force gradient at  $r = R$ , gives the constraint

$$\Delta t < \frac{R}{2} [\max(\langle v_{r+} \rangle, \langle v_{r-} \rangle)]^{-1}. \quad (3.34)$$

## 3.5 Smoothing techniques

Explicit numerical solvers are always subject to unwanted oscillations, caused by discontinuities in the solution or derivatives. For example, the change of the magnetic field



over time is the negative curl of the electric field, making the magnetic field sensitive to oscillations.

All models have different schemes to deal with these in some non-physical way. In this hybrid model, the smoothing of numerical oscillations comes into the term  $\eta \mathbf{J}$ , of the electric field.

For the advancement in time for the magnetic field, Faraday's law is used (Equation 2.119). The magnetic Reynolds number,  $R_m$ , is used as a way to determine which term dominates the equation, which with dimensional analysis becomes

$$R_m = \frac{|\text{convective term}|}{|\text{diffusive term}|} = \frac{|\nabla \times (\mathbf{u} \times \mathbf{B})|}{\left| \nabla \times \left( \frac{\eta}{\mu_0} \nabla \times \mathbf{B} \right) \right|} \approx \frac{L u \mu_0}{\eta}, \quad (3.35)$$

where  $L$  is the typical length scale,  $u$  the bulk speed of the plasma, and  $\eta$  the resistivity. If  $R_m$  is large, the magnetic field is “frozen in” to the bulk plasma; the magnetic field convects with the plasma.

#### 3.5.1 Vacuum regions

When handling vacuum regions [21], the resistivity should be chosen as high as possible, such that diffusion dominates on the length scale of the vacuum region, making the Reynolds number small when comparing with the convective speed,  $u$ , of the ambient plasma.

If a vacuum region is comparable to the size of a body of radius  $R$ , the vacuum resistivity should at least satisfy,  $\eta_v > \mu_0 u R$ , for a physical solution. The same applies to a resistive body with its resistivity profile,  $\eta (r < R)$ .

Physically, the vacuum resistivity should be as high as possible, but for computational efficiency the exact opposite applies because of the time step constraint from Equation 3.30.

#### 3.5.2 Oscillations in the plasma

The plasma resistivity profile,  $\eta (r > R)$ , can be used to smooth numerical oscillations, by enforcing diffusion, in the magnetic field of the plasma.

To do this in the most physically correct manner possible, the resistivity should be sufficiently small such that the magnetic field is not dominated by diffusion on the order of the smallest length scale of the system, the cell size, i.e. the Reynolds number should

be high. The plasma resistivity should at least satisfy the frozen-in condition

$$\eta(r > R) < \mu_0 u \Delta x, \quad (3.36)$$

on the order of the cell size.

By setting the constraints for the time steps equal from the previous section, one can see that for smoothing any wave with phase speed  $v_{\text{ph}}$  on the length scale of the cell size needs a resistivity of

$$\eta > \frac{\sqrt{3} \mu_0 v_{\text{ph}} \Delta x}{2}, \quad (3.37)$$

being linear in cell size. By comparing Equations 3.36 and 3.37, it is easy to see that both conditions can only be valid if  $v_{\text{ph}} \gtrsim u$ , approximately. Waves travelling faster than the bulk plasma are easy to smooth without having to make the diffusive term of Faraday's law large. Therefore, a fast wave can be dampened without changing the evolution of the magnetic field as a whole. This is useful when dealing with sub-Alfvénic plasmas (discussed in Section 3.10), where the Alfvén waves can create substantial numerical oscillations.

Analogously, an oscillation of frequency  $\omega$  needs a resistivity of

$$\eta > \frac{\sqrt{3} \mu_0 \omega \Delta x^2}{2\pi}. \quad (3.38)$$

For any oscillation though, it is clear that for smaller cell sizes, the oscillation becomes easier to diffuse, without changing the frozen-in condition of the plasma.

### 3.5.3 Hyperresistivity

There are more ways of smoothing a solution, and one is to expand the resistivity into higher order terms of the Laplacian of  $\mathbf{J}$  [37]. By admitting one more term, the resistive term of the electric field (and Lorentz force) becomes

$$\eta \mathbf{J} \mapsto \eta \mathbf{J} - \eta_h \nabla^{[2]} \mathbf{J}, \quad (3.39)$$

where  $\nabla^{[2]}$  is a discrete central difference operator giving  $\nabla^{[2]} \mathbf{J} = \left( \frac{\partial^2 J_x}{\partial x^2}, \frac{\partial^2 J_y}{\partial y^2}, \frac{\partial^2 J_z}{\partial z^2} \right)$  [21]. The higher the order of the diffusive terms one includes, the more effective they are at erasing small-scale structures without affecting the larger scale. Hyperresistivity is a useful tool to smooth numerical oscillations in a sub-Alfvénic plasma.

By including hyperresistivity, the maximum allowed time step due to diffusion (Equation 3.30) can become larger [37].

### 3.6 Magnetic induction model

Conductive bodies in space subject to a time-varying field of constant frequency,  $\omega_B$ , will get currents induced inside them, giving rise to a dipole magnetic field (see Section 2.4.1). This is the case for bodies inside planetary magnetospheres such as Callisto [53], where the magnetic field of the parent body rotates with a frequency of one revolution per parent day.

Since the dipole field and its evolution with time is given by the primary field in Equation 2.114, and since Faraday's law is a linear equation, one may split the total magnetic field,  $\mathbf{B} = \mathbf{b}_0 + \mathbf{B}_0(t) + \mathbf{B}_1(t)$  into two parts in the model.

Three model variables, GRBX, GRBY, GRBZ, contain the components of the external field,  $\mathbf{b}_0 + \mathbf{B}_0(t)$ , and three other variables, GBX1, GBY1, GBZ1, contain the induced field,  $\mathbf{B}_1(t)$ .

If the time scale of interest is much shorter than  $\omega_B^{-1}$ , then the induced field can be assumed to be constant in the model, which is the case for Callisto (see Paper I). The magnetic dipole representing the induced currents can be specified by setting its location and the magnetic moment (magnitude and direction).

Only the external field contained in GRBX, GRBY, GRBZ, is advanced in time by Faraday's law. The magnetic field used for particle motion in the Lorentz force is naturally the total magnetic field.

### 3.7 Neutral release model

An "atmosphereless" body such as Callisto (Paper II) or Ceres (Paper III) will have some production of neutrals at its surface, creating at least a tenuous exosphere (collisionless atmosphere). The possible sources are many, but some can be due to sublimation (outgassing of neutrals from within the surface), sputtering (plasma hits the surface and knocks away neutrals from the surface), or via plumes (cracks opening up to expose a collection of, e.g., liquid water or nitrogen). This collection of neutrals can then ionize due to, e.g., photoionization or electron impact ionization.

These outflows of neutrals can be modelled. Assume that one knows the production rate of neutrals,  $Q$ , over some area,  $A$ . Further assuming that the cloud of neutrals is Maxwellian distributed in velocities, and non-collisional at the surface, one may use the expressions described in Section 2.3 to describe the outflow.

### 3.7.1 Implementation

The speed of exospheric neutrals is much slower than the average speed of the ambient plasma. Since neutrals are not affected by the electromagnetic fields, it is useful to split the solver into several time periods, where one first lets the neutrals reach steady state before moving on and including the plasma and electromagnetic fields.

For each time period, the model uses different time steps,  $\Delta t_0 < \Delta t_1 < \Delta t_2$ :

1. The time period when letting neutrals reach steady state, using the time step  $\Delta t_2$ .
2. The time period when filling the simulation domain with ambient plasma keeping fields constant, using the time step  $\Delta t_1$ .
3. The time period when updating fields, and ionizing neutrals, using the time step  $\Delta t_0$ .

#### Initiation

The simulation domain is periodic in two spatial dimensions, with an inflow/outflow boundary in the other spatial dimension (usually  $x$ ). New plasma is inserted at the inflow boundary ( $+x$ ) and removed at the outflow boundary ( $-x$ ). The magnetic field is extrapolated to the outflow cells, and at the inflow boundary equal to the ambient homogeneous electromagnetic fields (given at the start of the simulation).

When the simulation is initiated, the ambient plasma is filled with macroparticles in all cells according to a Maxwellian distribution, in order to initiate and calculate the electric and magnetic fields during the first two time steps of the simulation,  $\Delta t_0$ , which has to satisfy all time step constraints of Section 3.4. After running for two time steps, the time periods described above (1–3) will start, beginning with (1).

#### Filling the domain with neutrals

The fields are set as constant and are not updating with time. The time step is increased to  $\Delta t_2$ , which should resolve the gravitational fields using the condition in Equation 3.33, and should also resolve the particle motion of neutrals on the grid from Equation 3.27 to get good statistics in each cell. Now, neutrals with weight (number of real particles per macroparticle),  $w$ , start to be launched from the given area,  $A$ . For every time step henceforth, the probability of removing a neutral from the simulation domain is checked,

$$P_{n \rightarrow d}(\Delta t) = 1 - \exp(-v_d \Delta t), \quad (3.40)$$

where  $v_d$  is the destruction rate of neutrals (see Equation 2.102 setting  $v_i = v_d$ ). All neutrals moving outside the simulation domain are removed (no periodic boundaries for neutrals because of the radial symmetry in the gravitational force).

#### Filling the domain with ambient plasma

When the neutrals have reached steady state,  $t \approx 2 v_d^{-1}$ , the time step is increased to  $\Delta t_1$  which has to satisfy the CFL condition of particle motion described in Equation 3.27, and ambient plasma starts filling the simulation domain. The domain is filled after a time of approximately  $t \approx X/u$ , where  $X$  is the size of the domain in  $x$ , and  $u$  the bulk speed of the plasma.

#### Ionization and updating the fields

Now the time step is lowered to its initial value  $\Delta t_0$  again, and the electromagnetic fields are updated and advanced each time step. Henceforth, each neutral particle of weight,  $w$ , will create a new macroparticle with weight,  $\varepsilon w$ , with a probability

$$P_{n \rightarrow i}(\Delta t) = \frac{v_i}{v_d} [1 - \exp(-\varepsilon^{-1} v_d \Delta t)], \quad (3.41)$$

where  $\varepsilon$  is an arbitrarily chosen positive real number, such that a satisfactory weight of the ionized particles is achieved (preferably similar to the ambient plasma). Note that the neutral macroparticle will not be removed from the simulation here since that is already taken care of in Equation 3.40.

#### 3.7.2 Neutral distribution

At every time step of the simulation, the neutrals need to be randomly generated somewhere on the source region of area,  $A$ , according to some velocity distribution.

Let origo be at the centre of the spherical body in question. The source of neutrals on the surface is given a vector,  $\mathbf{r}_0$ , which marks the centre of the source. Now the source region is set as a spherical cap identified by an angle,  $0 \leq \theta_{\max} \leq \pi$ , where all vectors on the surface of the object,  $\mathbf{r}$ , are part of the source region if  $\mathbf{r} \cdot \mathbf{r}_0 \geq r r_0 \cos \theta_{\max}$ . For example, setting  $\theta_{\max} = \pi$  gives the whole surface as a source region, while  $\theta = 0$  becomes a point source.

Assuming a homogeneous production across the source region, and a Maxwellian distribution of neutrals at the surface according to a constant temperature,  $T_n$ , and radial bulk

speed,  $u_n$ , the neutrals can be launched with a Monte Carlo method. The total number of macroparticles generated for each time step is  $N = Q\Delta t/w$ .

If instead of the production rate the number density of neutrals for the *full* Maxwellian is known at the surface, the production rate can still be derived via Equation 2.108.

### Particle positions

A surface of equal temperature can be assumed to have the same flux of particles, for every infinitesimal area on the source region. Therefore, the position of a neutral macroparticle can be randomly generated at any point on the source region. Here an algorithm is presented that ensures that each area segment of the source region contains an equal number of neutral macroparticles.

Let a neutral particle's initial position on the surface,  $\mathbf{r}'$ , be represented by the spherical coordinate system:

$$\begin{aligned} x' &= R \sin \theta \cos \phi, \\ y' &= R \sin \theta \sin \phi, \\ z' &= R \cos \theta, \end{aligned} \tag{3.42}$$

where the source region now has its centre at  $z' = R$  ( $\theta = 0$ ).

There should be an equal number of particles generated per unit area, which means that the probability density scales with the area segment,  $dA$ . An area segment on the surface of the object can be written as  $dA = r'^2 \sin \theta d\theta d\phi$ . The integrand,  $dA$ , is constant in  $\phi$ , but not in  $\theta$ .

Let  $p$  be a random number taken from the distribution  $[0, 1]$ . Since the integral of  $d\phi$  is linear, the angle  $\phi$  is weighted linearly in probability and becomes

$$\phi = \phi_{\min} + (\phi_{\max} - \phi_{\min}) p = 2\pi p, \tag{3.43}$$

with  $\phi_{\min} = 0$ , and  $\phi_{\max} = 2\pi$ .

Let  $p$  be another random number taken from the distribution  $[0, 1]$ . Since the integral of  $\sin \theta d\theta$  is  $-\cos \theta$ , it is  $\cos \theta$  that is weighted linearly in probability and becomes

$$\cos \theta = \cos \theta_{\min} + (\cos \theta_{\max} - \cos \theta_{\min}) p = 1 + (\cos \theta_{\max} - 1) p, \tag{3.44}$$

where  $\theta_{\min} = 0$ .

Now  $\sin \theta = \sqrt{1 - \cos^2 \theta}$ , and the particle position vector,  $\mathbf{r}'$ , is rotated such that  $\mathbf{z}' \rightarrow \mathbf{r}_0$ , and is now represented in the simulation coordinate system.

### Particle velocities

The neutrals on the surface can be assumed to be stationary and in thermal equilibrium with each other. The velocity distribution can as such be described by a Maxwellian distribution.

Since the source region by assumption has homogeneous temperature, the particles' velocities are picked randomly from a Maxwellian distribution (see Equation 2.84), with a bulk speed of neutrals,  $u_n = 0$ . The distribution is then specified only by the temperature at the surface of the body,  $T_n$ . Only positive velocities in the radial direction are considered, and are optimized using a Monte Carlo algorithm by Garcia [15].

## 3.8 Haser model

For a body with small mass and physical extension such as a comet (Paper IV), one can assume that a non-collisional neutral cloud around such an object will have constant velocities if their thermal velocities greatly exceed that of the escape velocity of the body,  $\langle v \rangle \gg v_{\text{esc}} = \sqrt{2GM/R}$ .

Even if collisions are present close to the body as is the case for a high production rate, the cloud will eventually expand and become non-collisional. From the exobase, the neutral number density can be calculated with the Haser model [18] from Equation 2.106, for a destruction rate of  $v_d$ , giving

$$n(r) = \frac{Q}{4\pi r^2 \langle v_{r+} \rangle} \exp \left[ -\frac{v_d (r - R)}{\langle v_{r+} \rangle} \right]. \quad (3.45)$$

Close to the surface of the comet,  $\langle v_{r+} \rangle$  will represent the mean radial speed of a Maxwellian given by the surface temperature of the body, and will increase further from the comet if the production rate is high enough to make it collisional [52], thus making the number density of neutrals higher close to the body. At the same time, the atmosphere will become optically thicker, resulting in a decrease of the photodestruction and photoionization rates [52].

Fortunately when modelling plasmas, this implies that the ion production rate,

$$q_i(r) = v_i n(r), \quad (3.46)$$

can be considered approximately correct for all  $r$  if  $\langle v_{r+} \rangle$  is set as a constant value equal to the mean radial speed at the exobase.

### 3.8.1 Implementation

The neutral distribution is taken directly from the analytical expression of Equation 3.45, and neutrals are therefore not modelled as kinetic particles. This makes the model more efficient and less time-consuming than the *neutral release model* from Section 3.7.

The simulation domain is filled with ambient plasma, and an initial homogeneous magnetic field is set throughout the domain.

The time step of the simulation,  $\Delta t$  is chosen such that all CFL conditions of Section 3.4 are fulfilled.

For each time step, in each cubic cell, ions are produced with the ion production rate  $q_i(r)$ , where  $r$  is taken at the centre of each cell. Because of this, the simulation domain should be chosen in such a way that origo is not placed in the centre of a cell (it should preferably be placed in a corner) to avoid an infinite production rate. This leads to some discrepancies for small  $r$ , and could be optimized with an integration of the ion production rate for each cell, at the cost of efficiency.

## 3.9 Averaging techniques

Averaging, e.g., number densities close to a boundary which absorbs particles, such as the surface of a body, will underestimate the real number density and flux of particles close to that body. In this section some techniques are presented that use average quantities to achieve a high precision interpolation.

Average quantities of the particle distribution are calculated in the centre of each grid cell, such as charge densities and average current densities for each species, resistivity, and so on.

Average quantities at a position which is not in the centre of a cell are interpolated between grid cells. This can be illustrated by having an imaginary cell drawn around the position of interest, with the position being in the centre of that imaginary cell (see Figure 3.1). For instance, the number density at an arbitrary position is weighted proportionally to the volume the imaginary cell has in the real simulation grid cells.

Assume that we are interested of a position in the corner of a simulation grid cell. The average quantity for this position would be an average over the values of all eight neighbouring cells.



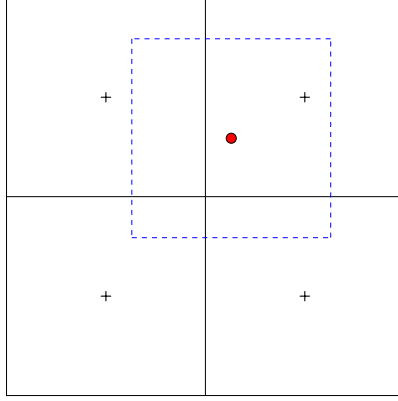


**Figure 3.1:** An average quantity is weighted proportionally to the volume enclosed by an imaginary cell around the position of interest. The figure only shows two dimensions. The central position is shown as a dot. The imaginary cell is shown as dashed lines. The simulation grid is outlined in solid lines. The cell centres of the grid are shown as plus signs. The maximum number of cells enclosed by the imaginary cell is eight.

Using the interpolation technique just explained close to an absorbing body's surface will only result in reliable results if one averages at a distance  $3\sqrt{3}\Delta x/2$  above the surface, thus ensuring that no grid cell enclosed by the imaginary cell is below the surface.

Instead, in post-processing of simulation data, the volume fraction which is outside the body of each neighbouring cell can be calculated numerically (or analytically). All macroscopic parameters proportional to the number density of particles are scaled proportionally to the volume fraction which is outside the body. This makes the results reliable down to a distance  $\sqrt{3}\Delta x/2$  above the surface, which ensures that the imaginary cell around any point is always above the surface. This technique has been used to generate number density and precipitation maps for Callisto (see Paper I and II). Averaging closer to the body than this is of course possible, but the grid structure then starts to be seen in the results.

This last described technique is not implemented in the hybrid solver itself, but could be implemented in the future to achieve greater precision of the charge density used when calculating in the electric field close to the body.

### 3.10 Sub-Alfvénic interaction

In planetary magnetospheres and extreme solar wind, the plasma flow can be sub-Alfvénic, meaning that the bulk flow of plasma is slower than the Alfvén and magnetosonic wave speeds,  $u < v_A < v_{MS}$ .

In this section, the implications of high wave propagation speeds are discussed. These affect the choices of the size and boundaries of the simulation domain, and have been taken into account when modelling the Jovian moon Callisto in Paper I and II.

For a supersonic plasma,  $u > v_S$ , the hybrid model has periodic boundaries in the  $y$ - and  $z$ -directions, and inflow/outflow boundary in  $x$  for plasma. Since the aim of most simulations is to reach a steady state solution, the domain size in the directions of the periodic boundaries has to be quite large compared to the flow direction of plasma in order to avoid waves returning into the simulation domain through the periodic boundaries.

Waves can also propagate upstream, reaching the inflow boundary and creating instabilities in the electromagnetic fields there because of the large gradients present due to the enforced ambient values in the inflow cells. The most accurate way to solve this is to also make the domain in  $+x$  large, at the cost of computational speed. If one is not physically interested in the wave propagation upstream, one may set a few layers of cells close to the inflow boundary to a higher plasma resistivity, resulting in diffusion of waves there and making it numerically stable.

#### 3.10.1 Subsonic interaction

In plasma environments where the thermal speed of the ambient plasma is larger or of the same order as the bulk speed,  $u < v_S$ , one can no longer use inflow/outflow boundaries. The part of the distribution moving opposite of the bulk velocity will only be represented initially in each cell of the simulation for such boundaries.

Instead, periodic boundaries should be used for all directions. This implies large domains if one aims for a steady-state solution where a body is immersed in the plasma. A region of steady-state plasma and fields would slowly expand outwards from the body in question for such a case.

Pure logical thinking cannot yield us any knowledge of the empirical world; all knowledge of reality starts from experience and ends in it.

---

Albert Einstein

## CHAPTER 4

# Plasma interactions with icy bodies

This chapter briefly summarizes the present knowledge of the plasma environments related to the icy bodies investigated in the included papers.

Characterizing the plasma around icy bodies is paramount in order to understand the plasma interaction with the bodies in question and their internal structures. This is best achieved by in situ measurements in the environments of the icy bodies themselves.

The Jovian system has been investigated by the spacecrafts *Pioneer 10 & 11* (flybys), *Voyager 1 & 2* (flybys), *Ulysses* (flyby), *Galileo* (orbiter), *New Horizons* (flyby), and will be visited again by the NASA orbiter *Juno* and the ESA orbiter *JUICE*.

The NASA orbiter *Dawn* is at the time of writing investigating the dwarf planet Ceres.

The comet 67P/Churyumov-Gerasimenko has been followed during its approach to and rounding of the Sun by the ESA orbiter *Rosetta*; the lander *Philae* descended onto the surface of the comet during the approach to the Sun.

Reaching an orbit around these bodies with a spacecraft requires lots of energy. Initially, the gravitational well of the Earth has to be overcome. Let us assume that from this point onwards, the spacecraft adjusts its speed such that it is momentarily kept in a circular orbit around the Sun at all times. The gravitational well from Earth can then be illustrated as in the diagram of Figure 4.1, which shows the accumulated speed-up ( $\Delta v$ ) needed in order to maintain a circular orbit at any heliocentric distance. Friction due to any atmosphere is not considered here. Parameters of masses, radii and distances have been taken from the references: [10, 50, 32, 34]. The blue dots mark the surfaces and the green dots the lowest orbit possible at the respective bodies. The red dots mark where the spacecraft is not gravitationally bound to that body. The comet 67P/Churyumov-Gerasimenko is left out on purpose because of its highly elliptic orbit.

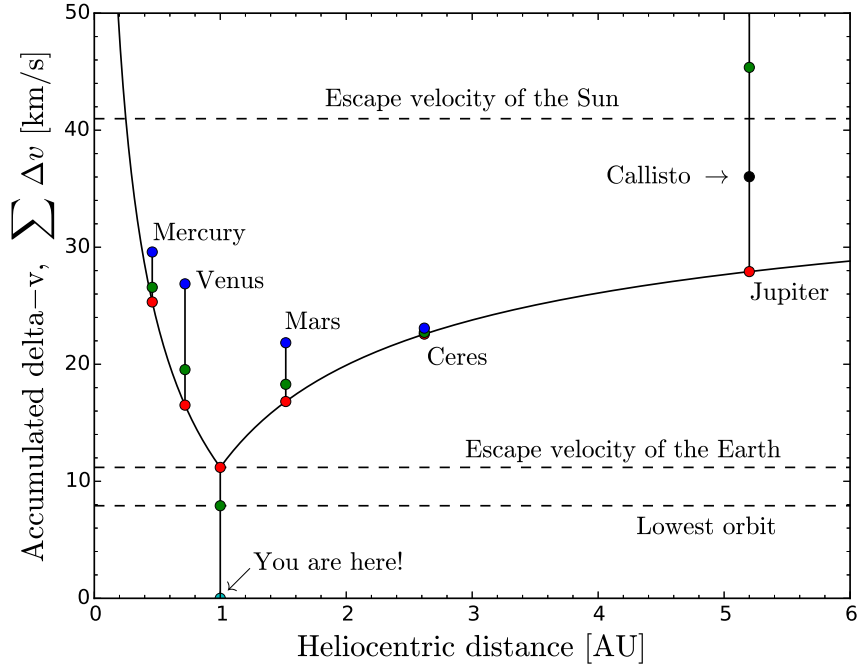


**Figure 4.1:** The gravitational well of the solar system ( $< 6$  AU) illustrated as the accumulated speed change needed for a spacecraft from Earth's surface,  $\sum \Delta v$ , in order to achieve a circular orbit around the Sun at any heliocentric distance. The blue dots mark the surfaces and the green dots the lowest orbit possible at the respective bodies. The red dots mark where the spacecraft is not gravitationally bound to that body. The black dot marks Callisto's circular orbit around Jupiter.

## 4.1 Solar wind

The solar wind is a multi-species, almost collisionless plasma, flowing supersonically radially outwards from the Sun at almost constant speed (from around the orbit of Venus and outwards). It consists mostly of protons and electrons.

Outside a few solar radii ( $\sim 10R_S$ ) [10], the dipole structure of the magnetic field of the Sun breaks down (called the source region). From here, only radial and azimuthal components of the magnetic field are present. The magnetic field becomes frozen in to the solar wind plasma, and has to convect together with it as it moves radially outwards.

Due to the rotation of the Sun around its own axis, the magnetic field will on average twist and create a *Parker spiral*. The magnetic field with respect to the plasma flow becomes

more perpendicular with increasing heliocentric distances.

The interplanetary magnetic field (IMF) far from the Sun forms an Archimedean spiral and is given by

$$\mathbf{B} = \pm B_0 \left( \frac{r_0}{r} \right)^2 \left( \hat{\mathbf{r}} - \frac{r \Omega_S \sin \theta}{u_{sw}} \hat{\phi} \right), \quad (4.1)$$

where  $r$  is the heliocentric distance,  $\theta$  is the inclination from the Sun's rotational axis,  $\hat{\phi}$  is the azimuthal unit vector,  $\Omega_S$  is the rotational frequency of the Sun in rad/s ( $2\pi/27$  days), and  $B_0$  is a reference radial magnetic field component at a distance  $r_0$ , which at the distance of Earth ( $r_0 = 1$  AU) has an approximate value of  $B_0 \approx 5$  nT [10]. The sign of the equation depends on whether one is above or below the heliospheric current sheet, and also on the dipole direction of the Sun which changes every 11 years.

The angle between the IMF and the radial direction (*IMF spiral angle*),  $\chi$ , is given by

$$\tan \chi = \frac{r \Omega_S \sin \theta}{u_{sw}}, \quad (4.2)$$

which for a typical solar wind bulk speed (400 km/s), at Earth ( $\theta = 90^\circ$ ,  $r_0 = 1$  AU) gets an approximate value of  $\chi \approx 45^\circ$  [10].

As can be seen, the magnetic field magnitude,

$$B = B_0 \left( \frac{r_0}{r} \right)^2 \sqrt{1 + \tan^2 \chi}, \quad (4.3)$$

has its highest value in the equatorial plane (where the planets orbit), for a given heliocentric distance,  $r$ . It can be noted that this is the exact opposite of a dipole field, which has the highest magnitude at the polar regions.

Since the solar wind bulk speed is on average constant after the orbit of Venus [10], the number density of the solar wind,  $n_{sw}$ , scales as  $1/r^2$  with heliocentric distances.

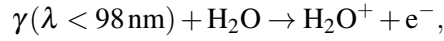
The solar wind interacts with all obstacles in its way, e.g., comets, asteroids, planets and their magnetospheres, and eventually the interstellar medium.

## 4.2 Comet 67P/CG

The target of the Rosetta mission, comet 67P/Churyumov-Gerasimenko (referred to as 67P/CG), is a Jupiter-family comet first detected in 1969 [8]. The orbital period of 67P/CG and its perihelion distance changed from 9.0 years and 2.7 AU to its present day value of 6.5 years and 1.3 AU, respectively, after a close encounter with Jupiter in 1959 [17].

As the comet approaches the Sun, a coma of vaporized ice,  $\text{H}_2\text{O}$ , and dust forms. Sunlight will break the parent water molecules apart. The end product depends on the wavelength of the photon interacting with the water. For an unattenuated (optically thin) medium the total rate of photodissociation of water, the photodestruction rate,  $\nu_d$ , by the Sun at 1 AU lies in the range  $1.26 \cdot 10^{-5} \text{ s}^{-1}$  (quiet Sun)  $< \nu_d < 2.30 \cdot 10^{-5} \text{ s}^{-1}$  (active Sun) [11], which also includes photoionization.

Only the extreme ultraviolet (EUV) part of the light spectrum,  $\lambda < 98 \text{ nm}$ , yields ionized water,  $\text{H}_2\text{O}^+$ , as an end product:



with the photoionization rate,  $\nu_i$ , in the range  $4.0 \cdot 10^{-7} \text{ s}^{-1}$  (quiet Sun)  $< \nu_i < 9.0 \cdot 10^{-7} \text{ s}^{-1}$  (active Sun) [11].

Since the intensity of solar radiation scales as  $1/r^2$  with heliocentric distance, so will the destruction/ionization rates of water.

Since the mass of the comet is small, the coma can be modelled with constant flux surfaces using the Haser model (see Section 2.3.3).

In Paper IV, a long-term study of solar wind protons is conducted for heliocentric distances  $> 2 \text{ AU}$  at the comet 67P/CG, where a low level of mass-loading is seen. These observations are compared with hybrid model results using the Haser model.

### 4.2.1 Evolution of the comet interaction

Consider scaled values with heliocentric distances of typical solar wind conditions (see Tables 4.1 and 4.2) [11, 10]. As the comet approaches the Sun, one can follow the evolution of the solar wind interaction with the comet in Figures 4.2, 4.3, 4.4, 4.5 and 4.6, where the hybrid model including the Haser model has been applied.

**Table 4.1:** Solar wind conditions used in the model for the comet 67P/CG.

$r \text{ [AU]}$	$n_{\text{sw}} \text{ [cm}^{-3}\text{]}$	$u_{\text{sw}} \text{ [km/s]}$	$B_0 \text{ [nT]}$	$\chi \text{ [}^\circ\text{]}$
2.7	0.7	400	2.0	70
2.35	0.9	400	2.3	67
2.0	1.25	400	2.8	63
1.65	1.85	400	3.5	59
1.3	3.0	400	4.9	52

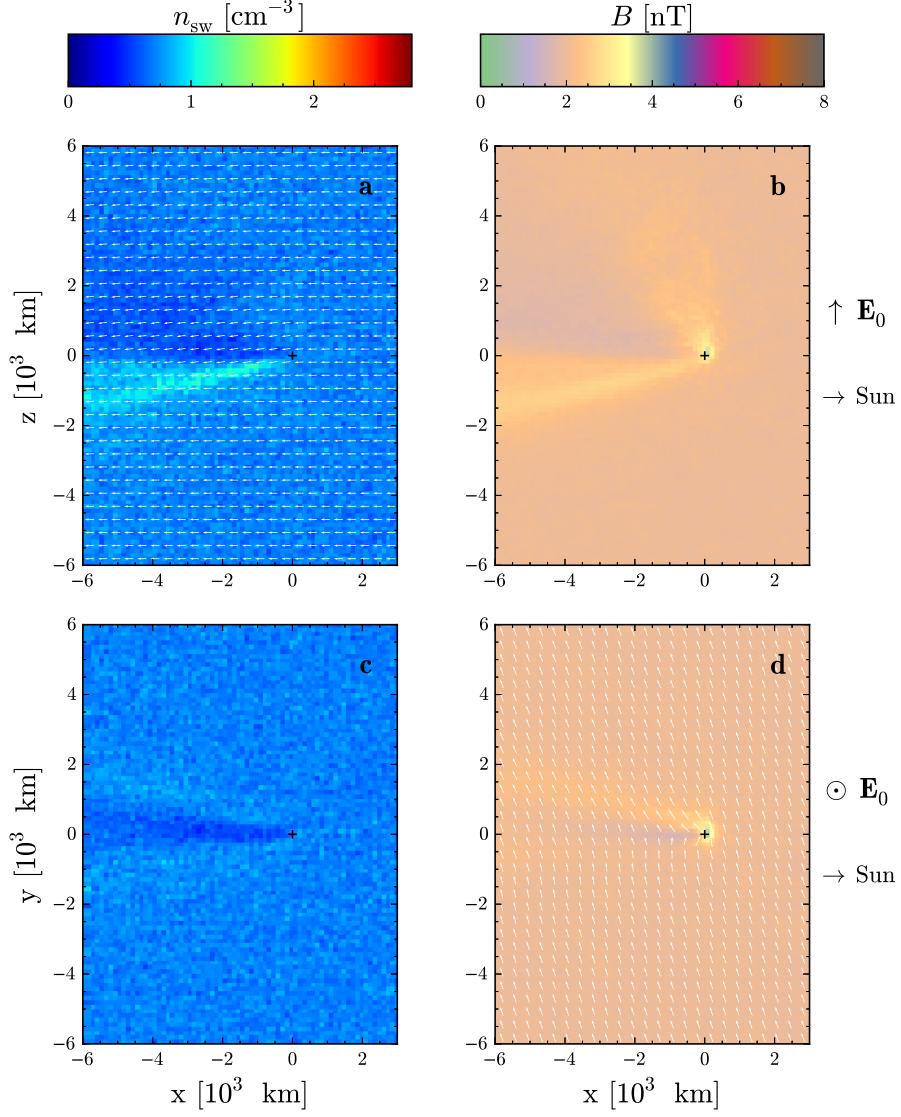


**Figure 4.2:** Hybrid model results including the Haser model for comet 67P/CG at 2.7 AU. Number density of solar wind protons (**a** and **c**) and the magnetic field magnitude (**b** and **d**). The vector field of the solar wind proton bulk velocity is shown in (**a**), and the magnetic field vector field in (**d**). The location of the comet is marked by black cross-hairs.

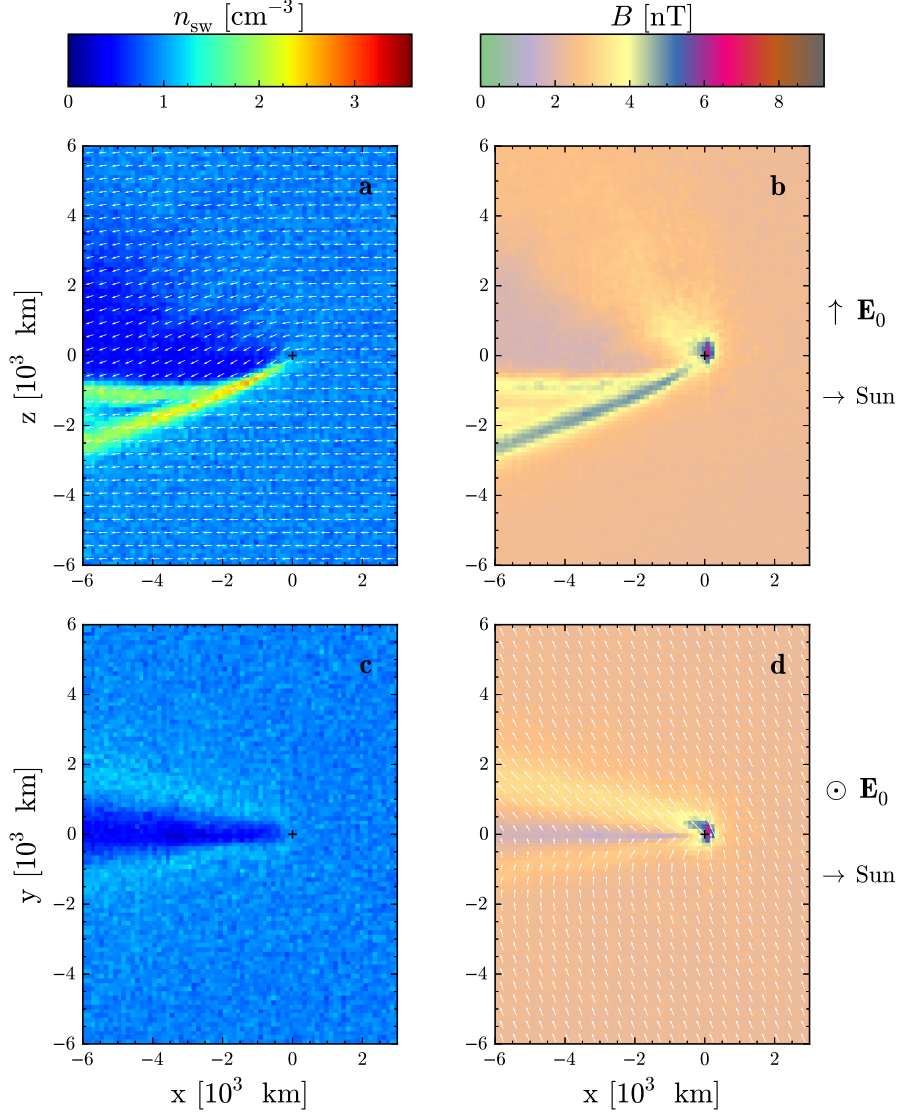


**Figure 4.3:** Hybrid model results including the Haser model for comet 67P/CG at 2.35 AU. Number density of solar wind protons (**a** and **c**) and the magnetic field magnitude (**b** and **d**). The vector field of the solar wind proton bulk velocity is shown in (**a**), and the magnetic field vector field in (**d**). The location of the comet is marked by black cross-hairs.



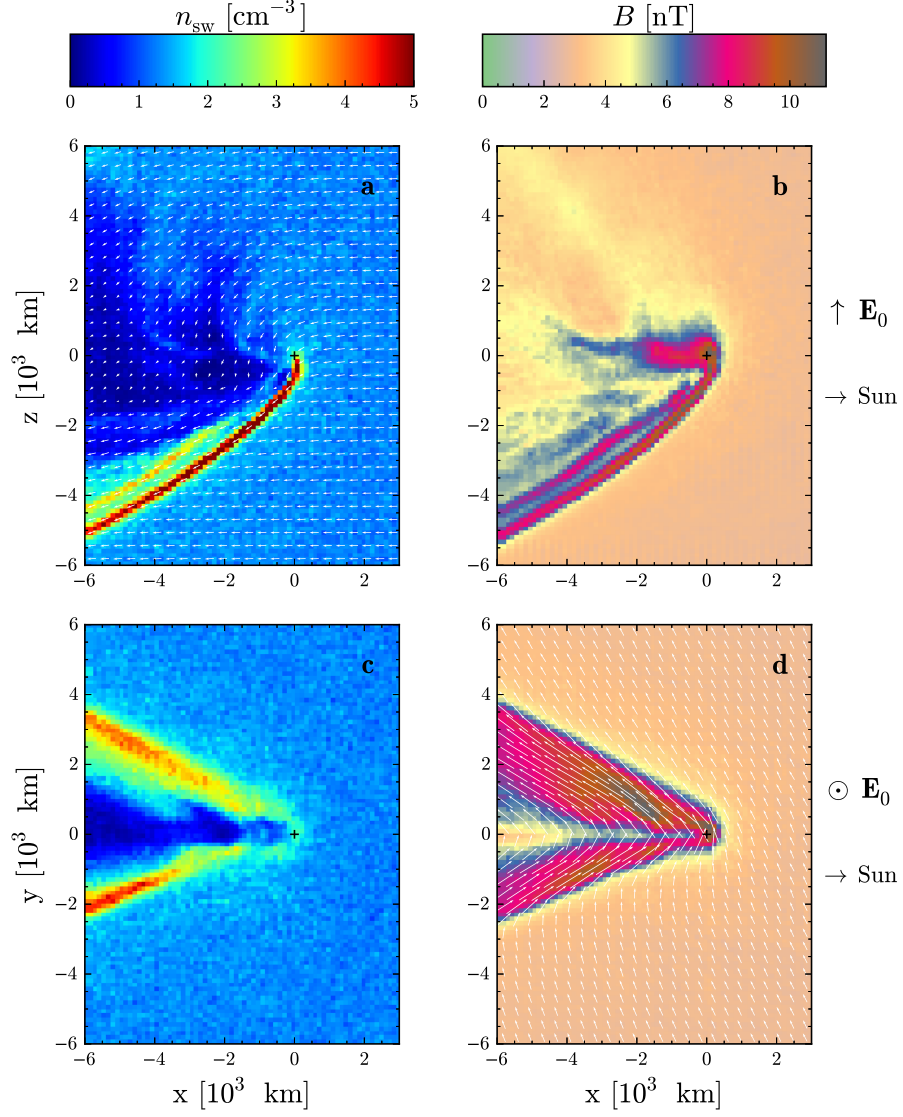


**Figure 4.4:** Hybrid model results including the Haser model for comet 67P/CG at 2.0 AU. Number density of solar wind protons (**a** and **c**) and the magnetic field magnitude (**b** and **d**). The vector field of the solar wind proton bulk velocity is shown in (**a**), and the magnetic field vector field in (**d**). The location of the comet is marked by black cross-hairs.

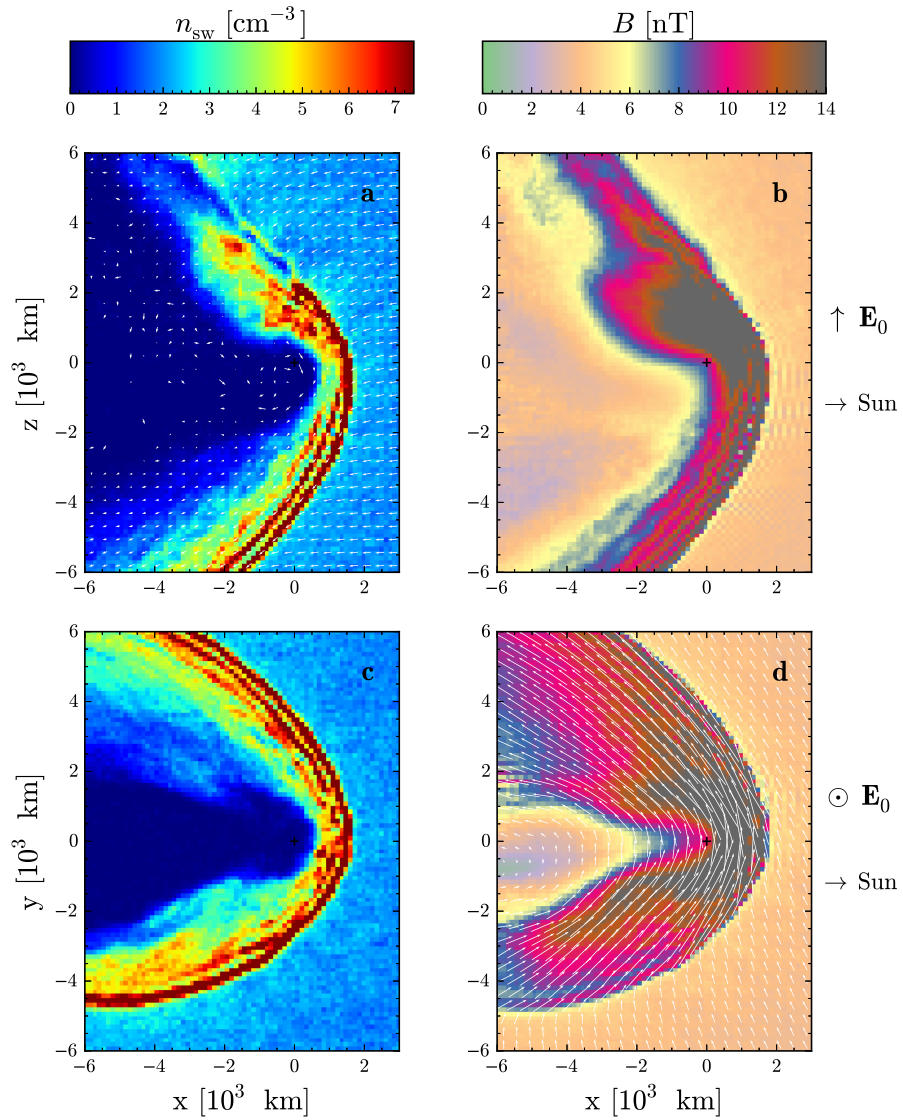


**Figure 4.5:** Hybrid model results including the Haser model for comet 67P/CG at 1.65 AU. Number density of solar wind protons (**a** and **c**) and the magnetic field magnitude (**b** and **d**). The vector field of the solar wind proton bulk velocity is shown in (**a**), and the magnetic field vector field in (**d**). The location of the comet is marked by black cross-hairs.

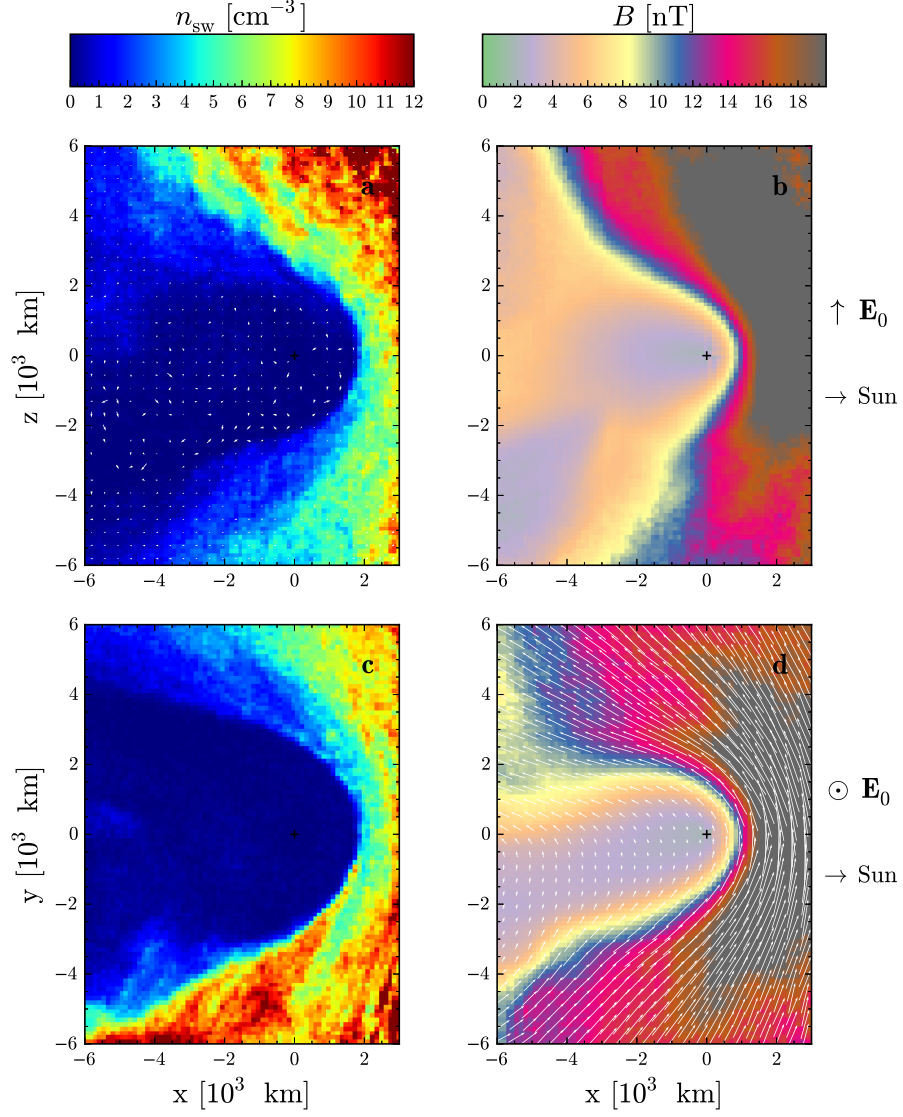


**Figure 4.6:** Hybrid model results including the Haser model for comet 67P/CG at 1.3 AU (perihelion). Number density of solar wind protons (**a** and **c**) and the magnetic field magnitude (**b** and **d**). The vector field of the solar wind proton bulk velocity is shown in (**a**), and the magnetic field vector field in (**d**). The location of the comet is marked by black cross-hairs.

**Table 4.2:** Cometary parameters used in the model for the comet 67P/CG.

$r$ [AU]	$u_n$ [km/s]	$Q$ [ $s^{-1}$ ]	$v_i$ [ $s^{-1}$ ]	$v_d$ [ $s^{-1}$ ]
2.7	0.7	$1.0 \cdot 10^{26}$	$8.9 \cdot 10^{-8}$	$2.4 \cdot 10^{-6}$
2.35	0.7	$2.7 \cdot 10^{26}$	$1.2 \cdot 10^{-7}$	$3.2 \cdot 10^{-6}$
2.0	0.7	$8.5 \cdot 10^{26}$	$1.6 \cdot 10^{-7}$	$4.5 \cdot 10^{-6}$
1.65	0.7	$3.3 \cdot 10^{27}$	$2.4 \cdot 10^{-7}$	$6.5 \cdot 10^{-6}$
1.3	0.7	$1.8 \cdot 10^{28}$	$3.8 \cdot 10^{-7}$	$1.1 \cdot 10^{-5}$

The solar wind flows in the  $-\hat{\mathbf{x}}$ -direction, with the ambient magnetic field as a Parker spiral in the  $xy$ -plane. The convective electric field is  $\mathbf{E}_0 = -\mathbf{u}_{sw} \times \mathbf{B}_0 = E_0 \hat{\mathbf{z}}$ . The simulation domain is  $|x| < 6 \cdot 10^3$  km,  $|y| < 12 \cdot 10^3$  km and  $|z| < 18 \cdot 10^3$  km.

The solar wind deflects more and more as the comet approaches the Sun, transferring momentum to the water ions, until eventually a bow shock is formed. Note that charge exchange and collisions are not considered here.

### 4.3 Ceres

Located in the main asteroid belt between the orbits of Mars and Jupiter, Ceres has through time been depleting the main belt of most of its original mass [41]. It is proposed that Ceres may originally have formed farther from the Sun, given its similarities with icy bodies in the outer solar system like Pluto [16].

Ceres has a quite low albedo of  $0.090 \pm 0.003$  [33], and if water ice is present on Ceres it is probably covered by a dust layer with a thickness of about 20 m or more [46]. The *Dawn* spacecraft in orbit around Ceres at the time of writing is making measurements of Ceres' gravity field; it is hoped that together with models, these will answer the question of whether a subsurface ocean might exist at Ceres. This is probably the case for other icy bodies such as Saturn's moon Enceladus and Jupiter's moon Europa [16].

Water vapour was detected at Ceres by the Herschel Space Observatory in 2012 and 2013 [32]. There, two regions located around Ceres' equator, Piazzzi (longitude  $123^\circ$ , latitude  $+21^\circ$ ) and Region A (longitude  $231^\circ$ , latitude  $+23^\circ$ ), were identified as originators of water vapour. Using radiative transfer modelling, the sublimation rate of water that best fits observations is a total of 6 kg/s ( $2 \cdot 10^{26}$   $H_2O$   $s^{-1}$ ), with 3 kg/s from each source [32]. Recent studies have estimated an upper limit on the production rate of  $4 \cdot 10^{26}$   $H_2O$   $s^{-1}$  [45].

The identification of more than one source suggests an outgassing from a small ice fraction

near the surface as opposed to sporadic activity triggered by a singular event like a recent large impact [32]. This supports the idea that Ceres possesses an icy mantle [32].

Subsurface sublimation of buried ice as first investigated by Fanale and Salvail in 1989 suggests a constant sublimation rate of the order of  $10^{24} \text{ H}_2\text{O s}^{-1}$  [12]. The discovery of the high outgassing events on the order of hours by the Herschel Space Observatory [32] has changed our view of the physical properties of Ceres.

In contrast to comets, the masses of which are much less than Ceres', its gravitational field will govern the dynamics of the exosphere. The exosphere will photoionize, and charged particles will be picked-up by the plasma flow, thus mass-loading the solar wind. Ceres' heliocentric distance lies in the approximate range  $2.5 \text{ AU} < r < 3 \text{ AU}$ , giving some variation of surface temperature and photoionization rates during its annual cycle. This is the same process happening at comets, but for more eccentric orbits.

The water vapour will ionize due to radiation and start to interact with the solar wind plasma. The interaction will depend on how the source of the water release is distributed on the surface; this is addressed in Paper III. Since Ceres rotates with one sidereal revolution in 9.074 hours [6], the active source regions will as well.

Close to Ceres, the large body makes an obstacle to the solar wind and creates a wake, an asymmetric wake in fact, since the solar wind deflects to conserve momentum by the newly inserted water ions to the solar wind flow. The interaction close to Ceres depends greatly on the source location of water vapour, whereas far from Ceres it does not. For a surface temperature of 235 K, the thermal velocities of the released water vapour are comparable to the escape velocity, and  $\sim 66$  percent will escape Ceres' gravitational field when neglecting collisions and photodissociation. On a global scale, Ceres has a comet-like interaction with the solar wind.

The global morphology of the interaction can be seen in Figure 4.7. There, the solar wind flows in the  $-\hat{\mathbf{x}}$ -direction, with the ambient magnetic field as a Parker spiral in the  $xy$ -plane. The convective electric field is  $\mathbf{E}_0 = -\mathbf{u}_{\text{sw}} \times \mathbf{B}_0 = E_0 \hat{\mathbf{z}}$ . The simulation domain is  $-288R < x < 96R$ ,  $|y| < 96R$  and  $|z| < 192R$ , where  $R = 476.2 \text{ km}$  is Ceres' radius.

Water ions are accelerated along the convective electric field,  $\hat{\mathbf{z}}$ , and enforces a deflection of the solar wind in the opposite direction,  $-\hat{\mathbf{z}}$ . The solar wind deflects up to  $15^\circ$  as can be seen in Figure 4.7a. The magnetic field and number density enhancements correspond to an asymmetric shock structure. The draping of magnetic field lines can be in the vector field of Figure 4.7d.

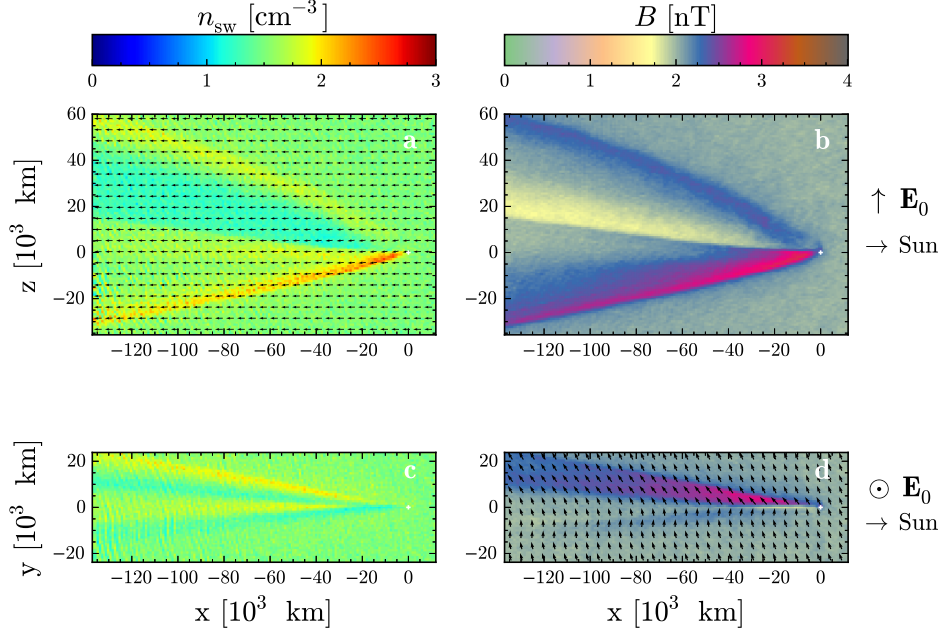


**Figure 4.7:** Hybrid model results including the Haser model for Ceres at 2.62 AU, during a high outgassing event corresponding to a water vapour production rate,  $Q = 2 \cdot 10^{26} \text{ H}_2\text{O s}^{-1}$ . Number density of solar wind protons (**a** and **c**) and the magnetic field magnitude (**b** and **d**). The vector field of the solar wind proton bulk velocity is shown in (**a**), and the magnetic field vector field in (**d**). The location of Ceres is marked by white cross-hairs. Ceres has a radius of 476.2 km.

## 4.4 Callisto

Callisto, Jupiter's second largest and outermost Galilean satellite, is only partially differentiated. It is heavily cratered and geologically inactive. Its surface is the oldest of all the Galilean satellites.

It possesses a thin atmosphere predominantly of  $\text{CO}_2$ , with a surface number density of  $\sim 4 \cdot 10^8 \text{ cm}^{-3}$ , and atmospheric scale height of about 23 km [5].

An ionosphere has been observed at Callisto with radio occultation measurements by the *Galileo* spacecraft [31]. The exosphere is ionized by both electron impacts and photons, and it is therefore argued that the ionosphere is greatest at the time when the

magnetospheric plasma of Jupiter hits Callisto on its sunlit side [31].

Callisto has no intrinsic magnetic field, but is conductive. We know this since Callisto's magnetic dipole field flips direction depending on which side of Jupiter's magnetic lobes it is located [27]. The induced currents are possibly due to a conductive subsurface ocean [27, 53, 34].

#### 4.4.1 The magnetosphere of Jupiter

The icy satellites Europa and Callisto, orbiting Jupiter, are two of the few solar system objects where induction has been observed to take place [27, 42, 29].

The induction is generated by a time-varying field, the origin of which is primarily the inclination of Jupiter's magnetic dipole moment with respect to Jupiter's spin axis by  $9.6^\circ$  [26].

Callisto is orbiting almost exactly in the equatorial plane of Jupiter's rotation [43]. Taking into account the prograde orbital velocity of Callisto,  $\sim 8$  km/s [28], the magnetic field that Callisto encounters will change with a synodic period of 10.1 h [30], giving an angular frequency of  $\omega_B = 1.728 \cdot 10^{-4}$  rad/s.

For a right-handed Callisto-centred coordinate system, let  $-\hat{\mathbf{x}}$  be the direction of rigid corotation,  $-\hat{\mathbf{y}}$  the direction of Jupiter seen from Callisto and with  $\hat{\mathbf{z}}$  parallel to Jupiter's spin axis. Jupiter's magnetic dipole field can be decomposed into a component anti-parallel to Jupiter's spin axis ( $-\hat{\mathbf{z}}$ ), and a component perpendicular to it ( $\pm\hat{\mathbf{y}}$ ). In reality, Jupiter's magnetic field is only a dipole field to a first-order approximation, and has in fact higher order terms and asymmetries related to, e.g., the solar wind interaction at the Jovian magnetopause and cusp regions, the rotation of Jupiter and the mass-loading by the satellite Io [26].

The dipole field component anti-parallel to the spin axis is rotationally symmetric in the equatorial plane where Callisto is situated, and will not vary with time ( $\mathbf{b}_0$  in Equation 2.111). The perpendicular time-varying component is called the primary field ( $\mathbf{B}_0(t)$  in Equation 2.111), and is responsible for the induction of currents inside the conductive Callisto.

In contrast to Earth, where most magnetospheric plasma originates from the solar wind, most of the plasma in the Jovian magnetosphere comes from the Jovian system itself. Io, the Galilean moon orbiting closest to Jupiter, is geologically active and its volcanic activity is continuously filling the magnetosphere with mostly sulphuric dioxide,  $\text{SO}_2$  [39], making  $\text{S}^+$ ,  $\text{S}^{++}$ ,  $\text{O}^+$  and  $\text{O}^{++}$  the dominant species of the magnetospheric plasma [2]. At the orbit of Callisto, oxygen is the dominant ion species [40, 3].

The magnetospheric plasma is almost corotating with Jupiter, and is moving with a relative velocity  $-192 \hat{x}$  km/s at the orbit of Callisto [28]. This means that the bulk of the magnetospheric plasma hits the trailing hemisphere of Callisto in its orbit around Jupiter.

The ambient plasma and field parameters depend greatly on where Callisto is situated in the magnetosphere of Jupiter. During one rotation of Jupiter, Callisto will be in the magnetic equator twice, where the plasma density is higher [28], and the magnetic field magnitude is lower [26], compared to the magnetic lobes. This results in a high Alfvénic Mach number in the magnetic equator, while the opposite is true when Callisto is in the magnetic lobe. The Alfvénic Mach number falls somewhere in the approximate range  $0.02 \text{ (lobe min)} < M_A < 8.5 \text{ (equator max)}$ , with extreme values for bulk plasma speed, magnetic field magnitude and ion densities from the summarized values in [28].

### **Magnetic lobes**

In the magnetic lobes, the total magnetic field is dominated by the  $y$ -component, and thus the primary field, especially on the night-side magnetosphere of Jupiter. Currents are induced inside the conductive Callisto (see Section 2.4.1 and Paper I), generating a dipole magnetic field.

### **Magnetic equator**

In the magnetic equator, the primary field is close to zero and no dipole is induced in Callisto (see Section 2.4.2). Currents are induced in the body in the direction of the convective electric field of the Jovian magnetospheric plasma. A current is then carried in the plasma along the draped magnetic field lines.

## **4.4.2 Supersonic interaction**

The plasma environment around Callisto varies depending on where Callisto is located in the magnetosphere of Jupiter, as previously mentioned.

In this subsection, the magnetospheric plasma interaction with the conductive Callisto is compared for different types of plasma parameters summarized in Table 4.3, where extreme conditions have been used to fit the study [28, 53].

We conduct a parameter study of the plasma interaction with Callisto for a supersonic Mach number of  $M_S = 4.1$ . We have one case without an induced magnetic dipole, but with Callisto having a homogeneous resistivity,  $\eta(r < R) = 0.36 \text{ Ohm m}$  (suggested value



#### 4.4. CALLISTO

**Table 4.3:** Plasma parameters used in the model for Callisto. A line denotes an unchanged value.

Parameter	Notation	Unit	<b>a</b>	<b>b</b>	<b>c</b>	<b>d</b>
External field	$\mathbf{b}_0$	nT	(0,0,-40)	(0,0,-5)	(0,0,-40)	(0,0,-5)
Primary field	$\mathbf{B}_0$	nT	(0,0,-40)	(0,0,-5)	(0,0,-40)	(0,0,-5)
Ion number density	$n_0$	$\text{cm}^{-3}$	0.7	-	-	-
Plasma bulk velocity	$u_0$	km/s	130	-	-	-
Ion mass	$m_i$	amu	16	-	-	-
Electron temperature	$T_e$	eV	50	-	-	-
Ion temperature	$T_i$	eV	50	-	-	-
Thermal gyroradius	$r_g$	km	102	814	102	814
Gyration time	$t_g$	s	26	208	26	208
Dipole amplitude	$A$		0	0	1	1
Sonic Mach number	$M_S$		4.1	-	-	-
Alfvén Mach number	$M_A$		0.50	4.0	0.50	4.0
MS Mach number	$M_{MS}$		0.49	2.9	0.49	2.9

for a subsurface ocean [53]). In another case, Callisto has an induced magnetic dipole of amplitude,  $A = 1$  (within the constraint given in previous studies [53]). The magnetic field is also varied between 5 and 40 nT, resulting in sub-Alfvénic and super-Alfvénic cases. The simulation domain is  $|x| < 6R$ ,  $|x| < 12R$  and  $|z| < 18R$ , where  $R = 2410$  km is Callisto’s radius.

In Figures 4.8 and 4.9 the magnetic field magnitude and number density of the magnetospheric plasma is shown. In the sub-Alfvénic cases (strong magnetic field), the magnetic field is only mildly perturbed. Here, one can see that the magnetic field is enhanced both upstream and downstream of Callisto for the case with a dipole (**c**), but with a lower magnitude at the poles. For the case without a dipole (**a**) the magnetic field is piling up upstream of Callisto, draping around the body, and then being relaxed downstream.

The case that fits best for when Callisto is located in the magnetic equator corresponds to case **b** (weaker magnetic field and no induced dipole), where the field is draping and is significantly enhanced. The case corresponding best to the magnetic lobes is case **c** (strong magnetic field and an induced dipole), where the effect of the dipole is dominant and the field is barely affected by the plasma flow. The structure of the ion wake is changing between: small wake (**c**), elongated wake (**d**), broad wake (**a**) and a shock structure in (**b**). Upstream of Callisto for the sub-Alfvénic cases (**a** and **c**), the number density increases.

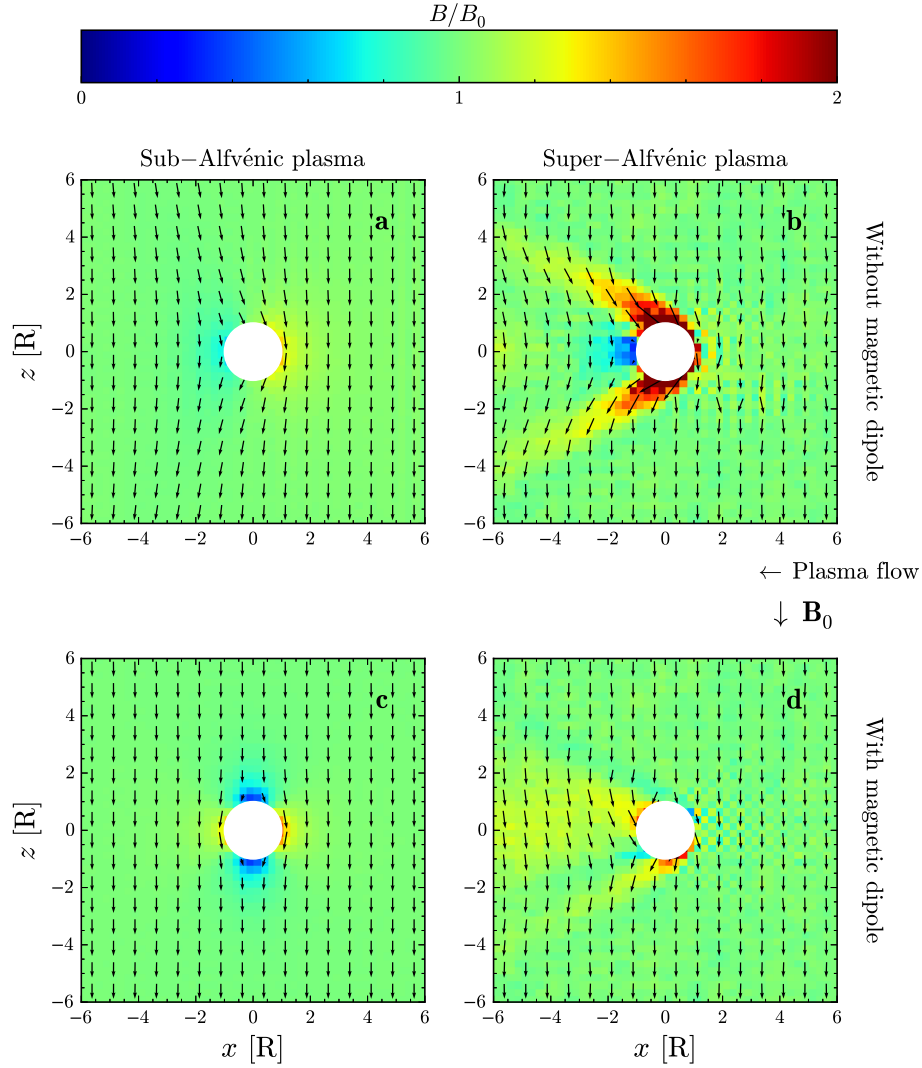


**Figure 4.8:** Hybrid model results of the magnetic field magnitude at Callisto. Sub-Alfvénic plasma without magnetic dipole (a). Super-Alfvénic plasma without magnetic dipole (b). Sub-Alfvénic plasma with magnetic dipole (c). Super-Alfvénic plasma with magnetic dipole (d). The magnetic field is also shown as a vector field. Callisto is shown in white. The axes are given in terms of Callisto's radius,  $R = 2410$  km.

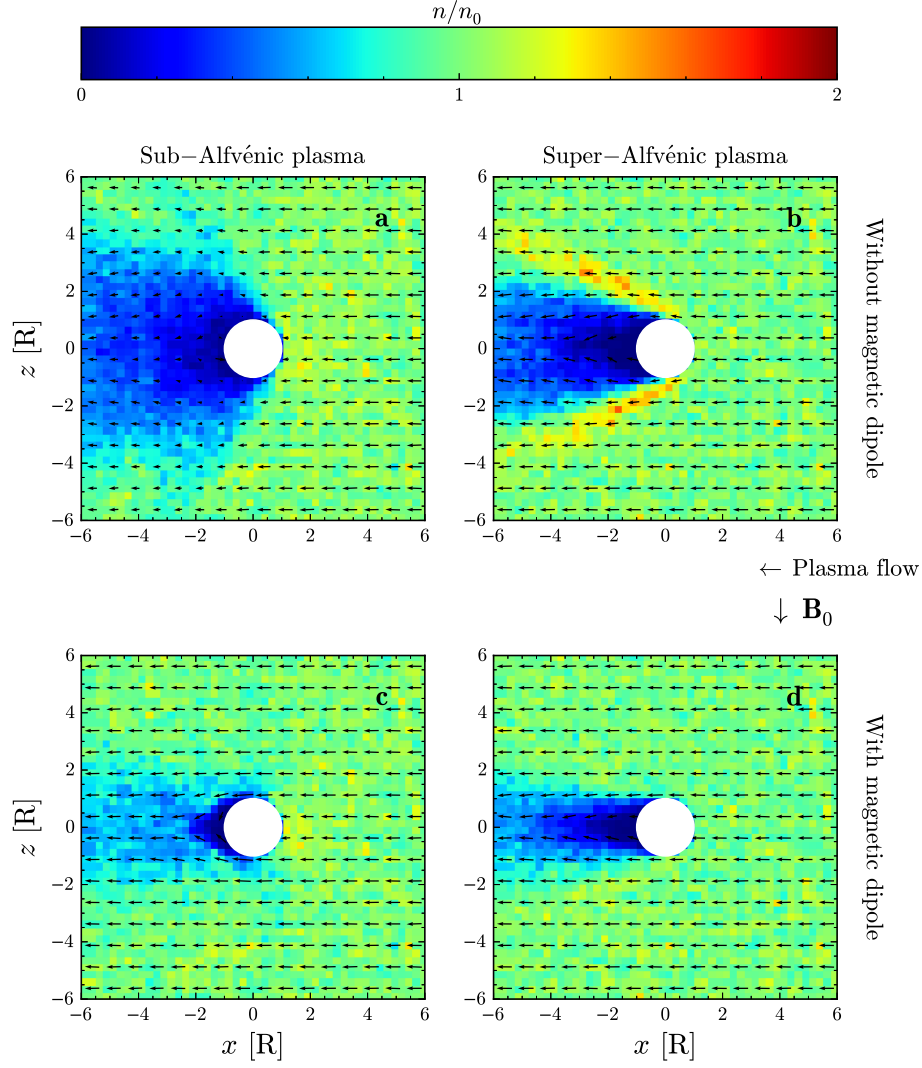


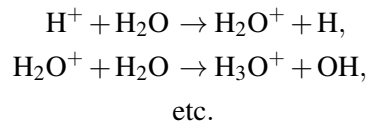
**Figure 4.9:** Hybrid model results of the ion number density at Callisto. Sub-Alfvénic plasma without magnetic dipole (a). Super-Alfvénic plasma without magnetic dipole (b). Sub-Alfvénic plasma with magnetic dipole (c). Super-Alfvénic plasma with magnetic dipole (d). The plasma bulk velocity is shown as a vector field. Callisto is shown in white. The axes are given in terms of Callisto's radius,  $R = 2410$  km.

## 4.5 Future work

### 4.5.1 Comet 67P/CG

We have investigated the plasma interaction with the comet during a period of low mass-loading of water ions, using the Haser model introduced in Section 3.8.

For a really dense coma, when the comet draws nearer to the Sun, other processes like charge-exchange need to be taken into account for all involved species:



Collisions in general make the Haser model insufficient to explain the full dynamics of the neutral coma and the ions.

### 4.5.2 Ceres

The high outgassing of water vapour from Ceres' surface is localized to small source regions [32], suggested to be due to subsurface sublimation [14]. Modelling the rotating sources assuming sublimation-driven outgassing and including a surface/subsurface temperature dependence could give a better view of the interaction as a preparation for a future plasma-dedicated mission to the asteroid main belt and Ceres.

The effects on the plasma interaction for a constant sublimation rate of the order of  $10^{24} \text{ H}_2\text{O s}^{-1}$  [12], should be investigated in the future. This could be conducted using an exosphere model including temperature-dependent cold-traps [51] and photoionization.

### 4.5.3 Callisto

The C30 *Galileo* flyby occurred when Callisto was in the magnetic equator of Jupiter, where the effect of a magnetic dipole is weakest; this is a prime suggestion for future research of the plasma interaction with Callisto, containing comparisons between model and observations.

The effects on the plasma interaction by an atmosphere/ionosphere has been recently studied [36]. A future model including both the effects of an ionosphere and the effects of a conducting subsurface ocean could be applied and compared with observations, e.g., from the C30 flyby.

## 4.6 Conclusions

The plasma interactions with icy bodies is very dynamic and complex. The icy bodies studied in this thesis are very diverse: from the super-Alfvénic and comet-like solar wind interaction with the large dwarf planet Ceres and the small comet 67P/CG, to the sub-Alfvénic magnetospheric interaction with the conductive moon Callisto, orbiting Jupiter.

The coma of comet 67P/Churyumov-Gerasimenko grows larger as the comet approaches the Sun, mass-loading the solar wind. Increased mass-loading of water ions causes the solar wind to deflect more, in order to conserve the total momentum.

Ceres has a comet-like interaction with the solar wind during the observed high outgassing events of water vapour, perturbing the solar wind far downstream of the body.

We have shown that Callisto acts as a conductor in its plasma environment, perturbing the magnetospheric plasma. Callisto has a tenuous atmosphere that will ionize, and could thus affect the plasma interaction.



'Forty-two,' said Deep Thought, with infinite majesty and calm.

---

Douglas Adams, *The Hitch Hiker's Guide to the Galaxy*

## CHAPTER 5

# Summary of included papers

### Paper I

#### **Callisto plasma interactions: Hybrid modeling including induction by a subsurface ocean**

The interaction between Callisto and Jupiter's magnetosphere for variable ambient plasma parameters was modelled. The results were compared with magnetometer data from the flybys: C3, C9 and C10 by the *Galileo* spacecraft. The magnetic field perturbations observed by *Galileo* correspond to induced currents inside Callisto, thought to be related to a subsurface ocean. Using typical upstream conditions of the magnetospheric plasma and including a magnetic dipole corresponding to the inductive response inside Callisto, we show that the model results agree well with the C3 and C9 flybys, but agree poorly with the C10 flyby close to Callisto.

#### **My contributions to Paper I**

I made simulation runs and analysed them. I wrote the text and provided all figures. I used already calibrated magnetometer data from the *Galileo* spacecraft which is publicly available via the NASA Planetary Data System (PDS) archive.

### **Paper II**

#### **3D-modeling of Callisto's sputtered exosphere environment**

This paper studies the release of various surface elements caused by plasma sputtering from an assumed icy and non-icy (i.e. chondritic) surface into the exosphere of Callisto. Hybrid modelling is applied to evaluate precipitation maps of the magnetospheric sputter agents  $H^+$ ,  $O^+$ , and  $S^+$ . The precipitation maps are applied to the assumed surface composition, where the related sputter yields are calculated by means of the 2013 SRIM code and coupled with a 3D exosphere model. The resulting exospheric particles' motion is modelled in Callisto's gravitational field, until they either escape the domain or hit the surface, where they are absorbed. The effects of collisions are discussed; these result in a tenuous atmosphere close to Callisto's surface.

#### **My contributions to Paper II**

I made simulation runs and provided data-sets of plasma parameters close to Callisto's surface, which were used as input in the study. I wrote the hybrid model description part of the paper. I provided code on how to plot Figure 1, which was adjusted later.

### **Paper III**

#### **Ceres interaction with the solar wind**

The solar wind interaction with Ceres is studied for a high vapour release from its surface, as observed by the Herschel Space Observatory on 6 March 2012. We modelled the interaction using a water vapour production rate from the surface of 6 kg/s. The photoionized water interacts strongly with the solar wind. Close to Ceres, the large body makes an obstacle to the solar wind and creates a wake, an asymmetric wake, since the solar wind deflects to conserve momentum by the newly ionized water molecules that accelerate along the convective electric field of the solar wind. The interaction close to Ceres depends greatly on the source location of water vapour, whereas far from Ceres it does not. On a global scale, Ceres has a comet-like interaction with the solar wind with observable disturbances farther than  $10^5$  km downstream of the body.



### **My contributions to Paper III**

I made simulation runs and analysed them. I wrote the text and provided all figures. I implemented a non-collisional exosphere model integrated in the hybrid model for arbitrary source regions. It contains a first-order photodissociation of water molecules, creating water ions.

### **Paper IV**

#### **Light mass loading of the solar wind at 67P/Churyumov-Gerasimenko**

A long term study of solar wind protons as seen by the *Rosetta* spacecraft was conducted as the comet 67P/Churyumov-Gerasimenko approached the Sun. Here, extreme ultraviolet radiation from the Sun ionizes the neutral water of the comet's coma. Newly produced water ions get picked-up by the solar wind flow and force the solar wind protons to deflect to conserve momentum. This effect increases steadily as the comet draws nearer to the Sun. The solar wind is deflected, but does not lose much energy. Hybrid modelling of the solar wind interaction with the coma agrees with the observations; the force acting to deflect the bulk of the solar wind plasma is greater than the force acting to slow it down.

### **My contributions to Paper IV**

I made simulation runs and analysis of the results. I wrote the model description part of the paper and parts of the results, discussions and conclusions. I provided two of the included figures.



# Acknowledgements

This work has been carried out at the Solar System Physics and Space Technology (SSPT) research group at the Swedish Institute of Space Physics (IRF) in Kiruna, under the supervision of Associate Professor Mats Holmström and Doctor Martin Wieser, led by the head of the research group and institute director Professor Stanislav Barabash. I would like to express my warmest thanks to them all.

I of course feel a special gratitude to Mats Holmström, my main supervisor, who somehow managed to lure me into research in this field and back to the north, to the land of the midnight sun!

I express my thanks to all co-authors, for their creative discussions and efforts which led to new frontiers of space.

I thank all co-workers at the Swedish Institute of Space Physics, the Department of Physics at Umeå University, the European Incoherent Scatter Scientific Association (EISCAT) headquarters and the Division of Space Technology at Luleå University of Technology in Kiruna.

I acknowledge funding and support from the Swedish National Space Board (SNSB), the National Graduate School of Scientific Computing (NGSSC), Uppsala University, and the Royal Swedish Academy of Sciences (KVA).

This research was conducted using computer resources provided by the Swedish National Infrastructure for Computing (SNIC) at the High Performance Computing Center North (HPC2N), Umeå University.

The hybrid solver has been developed by Mats Holmström, and is part of the open FLASH software developed by the DOE NNSA-ASC OASCR Flash Center at the University of Chicago.

## ACKNOWLEDGEMENTS

---

I would also like to take this opportunity to especially thank the following people:

Joan Stude, my brother in arms, and confidant.

Charles Lue, with his remarkable innovation and enthusiasm.

Shahab Fatemi, with all his expertise and stimulating discussions.

Katarina Axelsson, with her kind heart and comfort.

Rikard Slapak, the one and only axe-wielding archaeologist.

Robin Ramstad, my friend since ages past. A wizard is never late!

Etienne Behar, with so much science to do, and so little time.

Moa Persson, now you have to carry the burden.

Hans Huybrighs, the deriving plume-guy who never left.

Audrey Schillings, the one from the other research group.

Xiao-Dong Wang, who always wants to see the flames grow bigger.

Georgios Nicolaou, the one-armed man.

Diana Rojas Castillo, the one who always returns a smile.

Manabu Shimoyama, the much-needed experimentalist.

Gabriella Stenberg Wieser, with the wave diagram I will never forget.

Yoshifumi Futaana, for sharing his knowledge on programming and Jupiter.

Hans Nilsson, with his calm demeanour and helpful ways.

Masatoshi Yamauchi, introducing cause and effect. Aliens?

Leif Kalla, where would I be without a system programmer?

Jonas Olsen, with his sense of proper art, designing the cover of this thesis.

Asta Pellinen Wannberg, the meteor expert. The search is on!

Rick McGregor, for his outstanding help with layout and finding typos.

Carina Kreku, the binder of what is known.

Carina Gunillasson, for help in all practical (and impractical!) matters.

Stefan Hedlund, the curator.

Anders Tjulin, for wonderful times in nature.

Richard Larsson, my fellow Linux user.

Alfredo Metere, my brother from another mother.

I thank my family and friends for their unconditional support.

I would also like to thank Iron Maiden for needfully clearing my head of unwanted junk on a regular basis, especially during the time of writing this thesis! Up the irons!

Last, but certainly not least, I would like to thank my beloved, Pegah Lotfian, for the warmth of her love, and without whom this work would not have been completed at all.

Fred Jesper Urban Lindkvist

# Bibliography

- [1] BAGDONAT, T., AND MOTSCHMANN, U. 3D Hybrid Simulation Code Using Curvilinear Coordinates. *Journal of Computational Physics* 183 (2002), 470–485.
- [2] BAGENAL, F. Plasma conditions inside Io’s orbit. *Journal of Geophysical Research* 90 (1985), 311–324.
- [3] BAGENAL, F., SHEMANSKY, D. E., MCNUTT JR., R. L., SCHREIER, R., AND EVIATAR, A. The abundance of O<sup>++</sup> in the Jovian magnetosphere. *Geophysical Research Letters* 19, 2 (1992), 79–82.
- [4] BAUMJOHANN, W., AND TREUMANN, R. A. *Basic Space Plasma Physics*. Imperial College Press, 2012.
- [5] CARLSON, R. W. A tenuous carbon dioxide atmosphere on Jupiter’s moon Callisto. *Science* 283 (1999), 820–821.
- [6] CHAMBERLAIN, M. A., SYKES, M. V., AND ESQUERDO, G. A. Ceres lightcurve analysis—Period determination. *Icarus* 188, 2 (2007), 451–456.
- [7] CHEN, F. C. *Introduction to Plasma Physics and Controlled Fusion*. Plenum Press, 1984.
- [8] CHURYUMOV, K. I., AND GERASIMENKO, S. I. Physical Observations of the Short-Period Comet 1969 IV. *Symposium - International Astronomical Union* 45 (1972), 27–34.
- [9] COURANT, R., FREDRICHs, K. O., AND LEWY, H. Über die Differenzengleichungen der Mathematischen Physik. *Mathematische Annalen* 100 (1928), 32–74.
- [10] CRAVENS, T. E. *Physics of Solar System Plasmas*. Cambridge University Press, 1997.
- [11] CROVISIER, J. The photodissociation of water in cometary atmospheres. *Astronomy and Astrophysics* 213 (1989), 459–464.
- [12] FANALE, F. P., AND SALVAIL, J. R. The water regime of asteroid (1) Ceres. *Icarus* 82, 1 (1989), 97–110.
- [13] FLASH. Flash Center for Computational Science. *University of Chicago and Collaborators*, <http://flash.uchicago.edu/site/index.shtml>.
- [14] FORMISANO, M., DE SANCTIS, M. C., MAGNI, G., FEDERICO, C., AND CAPRIA, M. T. Ceres water regime: surface temperature, water sublimation and transient exo(atmo)sphere. *MNRAS* 455 (2016), 1892–1904.

## BIBLIOGRAPHY

---

- [15] GARCIA, A. L. *Numerical Methods for Physics*, 2 ed. Prentice-Hall, Inc., 2000.
- [16] HAND, E. Dawn probe to look for a habitable ocean on Ceres. *Science* 347, 6224 (2015), 813–814.
- [17] HANNER, M. S., TEDESCO, E., TOKUNAGA, A. T., VEEDER, G. J., LESTER, D. F., WITTEBORN, F. C., BREGMAN, J. D., GRADIE, J., AND LEBOSKY, L. The Dust Coma of Periodic Comet Churyumov-Gerasimenko (1982 VIII). *Icarus* 64 (1985), 11–19.
- [18] HASER, L. Distribution d’intensité dans la tête d’une comète. *Bulletin de la Classe des Sciences de l’Académie Royale de Belgique* 43 (1957), 740–750.
- [19] HEWETT, D. W. A global method of solving the electron-field equations in a zero-inertia-electron-hybrid plasma simulation code. *Journal of Computational Physics* 38, 3 (1980), 378–395.
- [20] HOLMSTRÖM, M. Hybrid modeling of plasmas. *Springer Proceedings of ENUMATH, the 8th European Conference on Numerical Mathematics and Advanced Applications* (2010), 451–458.
- [21] HOLMSTRÖM, M. Handling vacuum regions in a hybrid plasma solver. *ASTRONUM-2012, ASP conference series*, 474 (2013), 202–207.
- [22] HOLMSTRÖM, M., FATEMI, S., FUTAANA, Y., AND NILSSON, H. The interaction between the Moon and the solar wind. *Earth, Planets and Space* 64, 2 (2012), 237–245.
- [23] HUTCHINSON, I. H. Ion Collection by Oblique Surfaces of an Object in a Transversely Flowing Strongly Magnetized Plasma. *Physical Review Letters* 101, 035004 (2008).
- [24] HUTCHINSON, I. H. Electron velocity distribution instability in magnetized plasma wakes and artificial electron mass. *Journal of Geophysical Research* 117, A3 (2012).
- [25] HUTCHINSON, I. H. Near-lunar proton velocity distribution explained by electrostatic acceleration. *Journal of Geophysical Research* 118, 5 (2013), 1825–1827.
- [26] KHURANA, K. K. Euler potential models of Jupiter’s magnetospheric field. *Journal of Geophysical Research* 102, A6 (1997), 11295–11306.
- [27] KHURANA, K. K., KIVELSON, M. G., STEVENSON, D. J., SCHUBERT, G., RUSSELL, C. T., WALKER, R. J., AND POLANSKEY, C. Induced magnetic fields as evidence for subsurface oceans in Europa and Callisto. *Nature* 395 (1998), 777–780.
- [28] KIVELSON, M. G., BAGENAL, F., KURTH, W. S., NEUBAUER, F. M., PARANICAS, C., AND SAUR, J. Magnetospheric Interactions with Satellites. In *Jupiter - The Planet, Satellites and Magnetosphere*. Cambridge University Press, 2004, ch. 21.
- [29] KIVELSON, M. G., KHURANA, K. K., RUSSELL, C. T., VOLWERK, M., WALKER, R. J., AND ZIMMER, C. Galileo magnetometer measurements: A stronger case for a subsurface ocean at Europa. *Science* 289, 5483 (2000), 1340–1343.
- [30] KIVELSON, M. G., KHURANA, K. K., STEVENSON, D. J., BENNETT, L., JOY, S., RUSSELL, C. T., WALKER, R. J., ZIMMER, C., AND POLANSKEY, C. Europa and Callisto: Induced or intrinsic fields in a periodically varying plasma environment. *Journal of Geophysical Research* 104, A3 (1999), 4609–4625.

- 
- [31] KLIORE, A. J., ANABTAWI, A., HERRERA, R. G., ASMAR, S. W., NAGY, A. F., HINSON, D. P., AND FLASAR, F. M. Ionosphere of Callisto from Galileo radio occultation observations. *Journal of Geophysical Research* 107, A11 (2002), 1407.
- [32] KÜPPERS, M., O’ROURKE, L., BOCKELÉE-MORVAN, D., ZAHKAROV, V., LEE, S., VON ALLMEN, P., CARRY, B., TEYSSIER, D., MARSTON, A., MÜLLER, T., CROVISIER, J., AND BARACUCCI, M. A. Localized sources of water vapour on the dwarf planet (1) Ceres. *Nature* 505 (2014), 525–527.
- [33] LI, J. Y., MCFADDEN, L. A., PARKER, J. W., YOUNG, E. F., STERN, S. A., THOMAS, P. C., RUSSELL, C. T., AND SYKES, M. V. Photometric analysis of 1 Ceres and surface mapping from HST observations. *Icarus* 182, 1 (2006), 143–160.
- [34] LINDKVIST, J., HOLMSTRÖM, M., KHURANA, K. K., FATEMI, S., AND BARABASH, S. Callisto plasma interactions: Hybrid modeling including induction by a subsurface ocean. *Journal of Geophysical Research: Space Physics* 120, 6 (2015), 4877–4889.
- [35] LIPATOV, A. S. *The Hybrid Multiscale Simulation Technology*. Springer-Verlag Berlin Heidelberg, 2002.
- [36] LIUZZO, L., FEYERABEND, M., SIMON, S., AND MOTSCHMANN, U. The impact of Callisto’s atmosphere on its plasma interaction with the Jovian magnetosphere. *Journal of Geophysical Research: Space Physics* 120 (2015).
- [37] MARON, J. L., MAC LOW, M. M., AND OISHI, J. S. A constrained-transport magnetohydrodynamics algorithm with near-spectral resolution. *The Astrophysical Journal* 677 (2008), 520–529.
- [38] MATTHEWS, A. P. Current advance method and cyclic leapfrog for 2D multispecies hybrid plasma simulations. *Journal of Computational Physics* 112 (1994), 102–116.
- [39] MCGRATH, M. A., LELLOUCH, E., STROBEL, D. F., FELDMAN, P. D., AND JOHNSON, R. E. Satellite Atmospheres. In *Jupiter - The Planet, Satellites and Magnetosphere*. Cambridge University Press, 2004, ch. 19.
- [40] MCNUTT JR., R. L., BELCHER, J. W., AND BRIDGE, H. S. Positive Ion Observations in the Middle Magnetosphere of Jupiter. *Journal of Geophysical Research* 86, A10 (1981), 8319–8342.
- [41] MORBIDELLI, A., BOTTKÉ, W. F., NESVORNÝ, D., AND LEVISON, H. F. Asteroids were born big. *Icarus* 204, 2 (2009), 558–573.
- [42] NEUBAUER, F. M. The sub-Alfvénic interaction of the Galilean satellites with the Jovian magnetosphere. *Journal of Geophysical Research* 103, E9 (1998), 19843–19866.
- [43] NEUBAUER, F. M. Alfvén wings and electromagnetic induction in the interiors: Europa and Callisto. *Journal of Geophysical Research* 104, A12 (1999), 28671–28684.
- [44] PRITCHETT, P. L. Particle-in-Cell Simulations of Magnetosphere Electrodynamics. *IEEE Transactions on Plasma Science* 28, 6 (2000).

## BIBLIOGRAPHY

---

- [45] ROTH, L., IVCHENKO, N., RETHERFORD, K. D., CUNNINGHAM, N. J., FELDMAN, P. D., SAUR, J., SPENCER, J. R., AND STROBEL, D. F. Constraints on an exosphere at Ceres from Hubble Space Telescope observations. *Geophysical Research Letters* 43 (2016).
- [46] ROUSSELOT, P., JEHIN, E., MANFROID, J., MOUSIS, O., DUMAS, C., CARRY, B., MARBOEUF, U., AND ZUCCONI, J. M. A Search for Water Vaporization on Ceres. *The Astronomical Journal* 142, 4 (2011).
- [47] RUSSELL, C. T. Interaction of the Galilean Moons with their plasma environments. *Planetary and Space Science* 53 (2005), 473–485.
- [48] SAUR, J., NEUBAUER, F. M., AND GLASSMEIER, K. H. Induced Magnetic Fields in Solar System Bodies. *Space Science Reviews* 152 (2010), 391–421.
- [49] SHEN, C. S. An Analytical Solution for Density Distribution in a Planetary Exosphere. *Journal of the Atmospheric Sciences* 20, 2 (1963), 69–72.
- [50] THOMAS, P. C., PARKER, J. W., MCFADDEN, L. A., RUSSELL, C. T., STERN, S. A., SYKES, M. V., AND YOUNG, E. F. Differentiation of the asteroid Ceres as revealed by its shape. *Nature* 437 (2005), 224–226.
- [51] TU, L., IP, W. H., AND WANG, Y. C. A Sublimation-driven Exospheric Model of Ceres. *Planetary and Space Science* 104 (2014), 157–162.
- [52] VIGREN, E., AND GALAND, M. Predictions of ion production rates and ion number densities within the diamagnetic cavity of comet 67P/Churyumov-Gerasimenko at perihelion. *The Astrophysical Journal* 772 (2013).
- [53] ZIMMER, C., KHURANA, K. K., AND KIVELSON, M. G. Subsurface Oceans on Europa and Callisto: Constraints from Galileo Magnetometer Observations. *Icarus* 147 (2000), 329–347.